IN-44-CR
33462

P.72

# INFRARED POWER CELLS FOR SATELLITE POWER CONVERSION

Final Report

By

Christopher J. Summers

A-3575

Physical Sciences Laboratory
Georgia Tech Research Institute
Georgia Institute of Technology
Atlanta, Georgia 30332

Contract No. NAG-3-442

March 1991

Prepared for

NASA-Lewis Research Center
Cleveland, Ohio 44135

## CONTENTS

Page Number

# 1. INTRODUCTION

During the last decade there has been an intensive investigation to develop practical solar cells for the direct conversion of sunlight into electrical power. At the present time solar cells with efficiencies greater than 20% have been developed. These achievements suggest that the feasibility of developing radiation power converters for other parts of the electromagnetic spectrum should be investigated. A particularly useful application would be to use the energy in the earth's emission spectrum to power low orbiting communication and observation satellites. Because the earth's emission spectrum peaks at approximately 10 μm this application requires the development of very efficient power cell converters for the infrared spectral region.

Another potential application for an infrared power cell is as a receiver in a system to radiatively transfer power over long distances. The use of microwave power generators and power converters has been shown to produce a very efficient power transmission system, but requires large collecting antenna. A laser power transmission system would offer significant advantages in reducing the size of the system. At present the most efficient lasers are the CO and $CO_2$ systems which operate at 5.3 and 10.6 μm, respectively. Thus, a infrared power transmission line also requires very efficient power cells for the 5-15 μm spectral region. It should also be noted that because of the earth's atmospheric transmission characteristics, these lasers could also be used to beam power from an earth based laser system to an orbiting satellite, as well as between satellites.

In this report we have performed an analytical investigation to assess the feasibility of long-wavelength power converters for the direct conversion of infrared radiation into electrical power. Because these devices need to operate between 5 and 30 um the only material system possible for this application is the HgCdTe system which is currently being developed for infrared detectors. Thus this study essentially combines solar cell and infrared detector theories and technologies.

The development of efficient solar cells has experienced several evolutionary stages and with increasing device complexity significant increases in efficiency have been obtained. For all these structures optimum performance is dependent on obtaining the best material parameters relevant to the functions of light detection and power conversion, specifically, the electron and hole concentrations, mobilities, lifetimes, and diffusion lengths. The efficiency of a solar cell is also dependent on the optical concentration system; a fact that becomes very important for laser-power conversion. As discussed by Henry[1], the relative importance of the various parameters and mechanisms that determine solar cell performance can be defined from models whose input parameters fully describe the total optical-electrical system, the device structure and material properties.

In this work we have applied these considerations to determine the efficiency and optimum bandgap energies of single and multiple bandgap infrared power cells sensitive to 5-20 μm radiation. The calculation follows the method developed by Henry and has been used to calculate the efficiency and power output of a cell viewing a perfect blackbody at 300 K and the actual earth's emission spectrum. However, to be exact this calculation requires a detailed knowledge of the characteristics of long-wavelength photocells. Thus a comprehensive model of small bandgap HgCdTe p-n junction devices was developed, in which, current theories are used to calculate the intrinsic charge-carrier concentrations, carrier mobilities, lifetimes and diffusion lengths, and the absorption coefficient.

This approach was also used to access the efficiency of HgCdTe power cells with bandgap energies corresponding to 5.3 and 10.6 μm for converting optical energy to electrical energy from high power carbon monoxide and carbon diode laser systems. These studies were performed as a function of power cell temperature and incident laser power.

# 2. THEORY OF TERRESTRIAL POWER CELL

A solar cell is essentially a large area p-n or n-p junction which converts an incident photon flux directly into electrical energy. The physical mechanisms that affect the efficiency of the cell are the same as those that control the performance of a photodiode detector. However, the optimization of the device is more severe because the cell must be operated to deliver maximum current in addition to maximum voltage. Thus it is essential to understand the basic material properties which control device properties, particularly the electron and hole concentrations, lifetimes, mobilities and diffusion lengths on each side of the p-n junction. For the HgCdTe alloy system these are very dependent on the energy gap and electronic band structure of these alloys. Because of the importance of these effects on diode properties, a brief review is first given of the electronic properties of these alloys.

## 2.1 Electronic and Optical Properties of HgCdTe Alloys.

### 2.1.1 Electronic Band Structure.

Numerous investigations of both semiconducting and semimetallic HgCdTe alloys have established that the electronic and optical properties of this system are well described by the Kane energy band model shown as an insert in Figure 1.[2] In a normal InSb-type semiconductor, the s-like $\Gamma_6$ level is the edge of the lowest-lying conduction band, and the p-like $\Gamma_8$ level is the edge of the highest

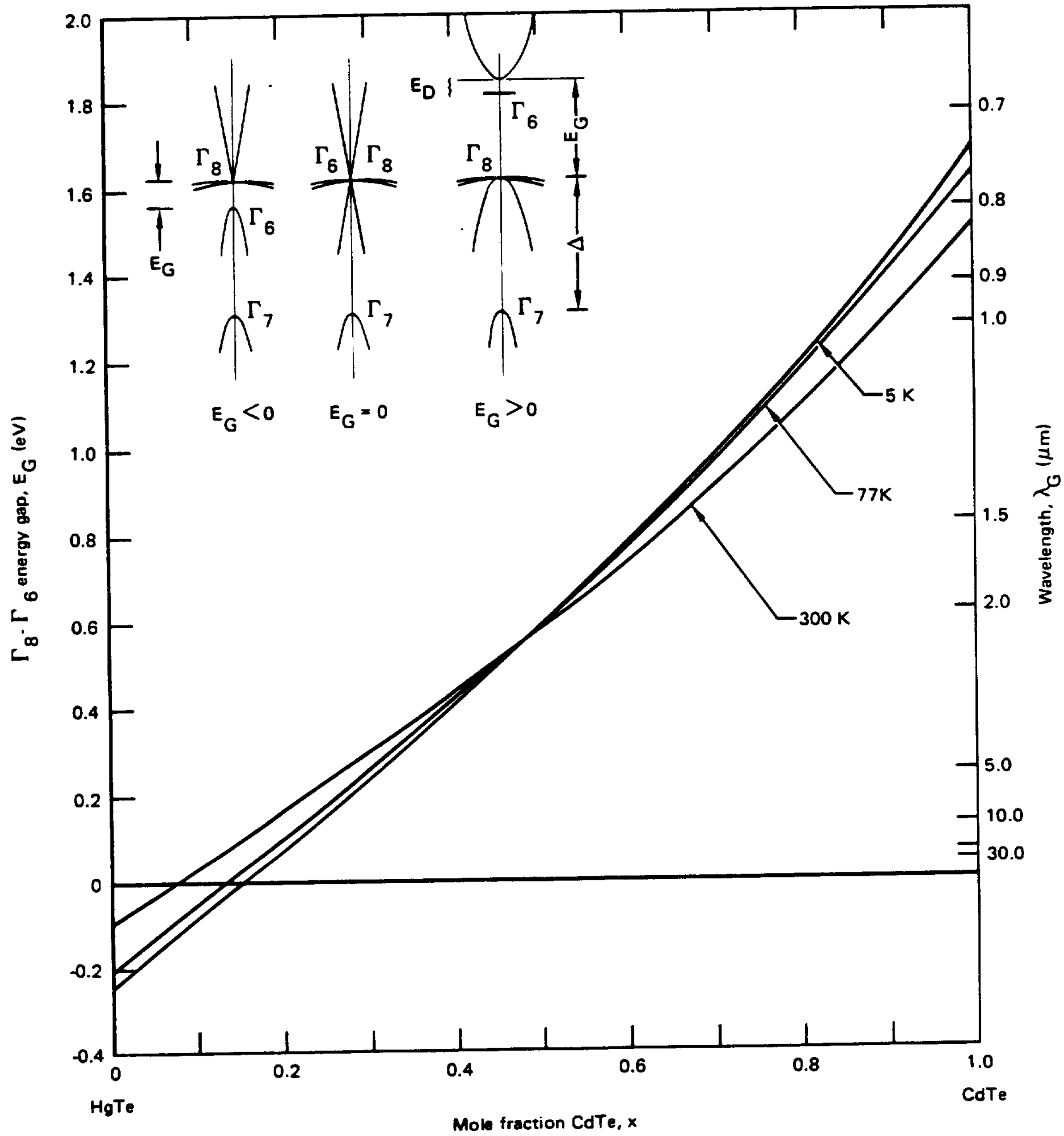

Figure 1. Dependence of energy bandgap on HgCdTe alloy composition and temperature.

valence band. The next valence band is the spin-orbit split-off $\Gamma_7$ bank. In the perfect semimetal structure, the $\Gamma_6$ level has fallen to a position between $\Gamma_9$ and $\Gamma_7$. Because $\Gamma_6$ and the light-hole part of the $\Gamma_8$ are k•p coupled, they invert; the light hole part of $\Gamma_8$ becoming a small-mass conduction band and $\Gamma_6$ becoming a valence band. The fundamental energy gap is therefore identically zero because the conduction and valence parts of $\Gamma_8$ are degenerate by symmetry.

In contrast, CdTe is a wide-gap semiconductor, and a simplified energy band model of the CdTe-HgTe pseudobinary alloy system is also shown in Figure 1. As the mole fraction, x, of CdTe is increased, the virtual-crystal $\Gamma_6$ level rises with respect to the $\Gamma_8$ level, crossing it at about x = 0.1. Above this critical value of x, the alloy is a normal Kane-type semiconductor. The energy-momentum (E-k) relationship of carriers in the conduction, light-hole and split-off bands are given by

$$E_n = E_n' + \frac{\hbar^2 k^2}{2m_o} \qquad (1)$$

where E are solutions of the secular equation

$$E^3 + (\Delta - E_G)E^2 - (E_G \Delta + p^2k^2)\ E - 2/3\ \Delta\ P^2k^2 = 0, \qquad (2)$$

and E, P and $\Delta$ are, respectively, the energy gap, momentum-matrix element and spin-orbit splitting at k = 0, and are empirical constants that must be determined experimentally. The heavy-hole band is assumed to be parabolic, i.e.,

$$E_{hh} = \frac{\hbar^2 k^2}{2 m_{hh} m_o} \tag{3}$$

where $m_{hh}$ is the heavy-hole effective mass which also be determined experimentally. The compositional and temperature dependence of the band structure follows as a consequence of substituting the experimentally determined functional dependences of $E_G$, P and $\Delta$ on the above variables in Equation 2. Of these parameters, $E_G$ is the most important as it determines the spectral range from the relationship:

$$\lambda_G = \frac{hc}{E_G} \tag{4}$$

and directly impacts values for carrier concentrations, mobilities, and lifetimes. For the range of alloy compositions, $0.13 < x < 0.6$ and temperatures, $20 < T < 300$ K, the compositional and temperature dependence of $E_G$ is;[3].

$$E_G = 0.25 + 1.59x + 5.233 \times 10^{-4}(1-2.08x)T + 0.327\ x^3 \tag{5}$$

where $E_G$ is in eV, and T is in Kelvins. This expression is plotted in Figure 1 as a function of alloy composition at 4.2, 77 and 300K, and shows that alloy compositions between 0.25 and 0.18 are required for the detection of radiation between 5 and 20 $\mu$m.

Figure 1 also demonstrates that $E_G$ is strongly dependent on both x and T for alloys operating at wavelengths longer than 10$\mu$m.

Values of P have been obtained from a variety of experimental investigations including gavanomagnetic, optical absorption and magneto-optical studies. For $0.0 < x < 0.7$ and $5 < T < 300$K the momentum-matrix element is independent of alloy composition and temperature and has the value,[4]

$$P = 8.4 \pm 0.2 \times 10^{-8} \text{ eV cm.} \tag{6}$$

The spin-orbit splitting is assumed to vary linearly between the values reported for HgTe and CdTe[5]

$$\Delta = 1.08 - 0.12 \, x \text{ eV.} \tag{7}$$

The heavy-hole effective mass for HgTe has been determined[6] as

$$m_{hh} = 0.55 \pm 0.03 \tag{8}$$

The reaction of charge carriers to applied fields is commonly described in terms of an effective mass, m*, which allows the particle-field interaction to be treated classically. In terms of the band structure shown in Figure 1

$$m^* = \hbar^2 \left( \frac{\delta^2 E}{\delta k^2} \right)^{-1} \tag{9}$$

The effective-masses are therefore dependent on energy, (carrier concentration) particularly in small band gap alloys, as demonstrated by the data shown in Figure 2. At k = 0 the conduction (electron) effective mass is given by

$$\frac{1}{m_c^*} = 1 + \frac{P^2}{3\hbar^2}\left(\frac{2}{E_G} + \frac{1}{E_G + \Delta}\right) \tag{10}$$

For device calculations it is also necessary to know the high- and low-frequency dielectric constants, which are found to be independent of temperature between 77 and 300K and to have the compositional dependence[7]:

$$\epsilon_O = 20.206 - 15.153x + 6.59x^2 - 0.952x^3 \tag{11}$$

and

$$\epsilon_\infty = 15.108 - 13.882x + 9.889x^2 - 3.671x^3 \tag{12}$$

The number of occupied conduction, light-hole, and heavy-hole states is:

$$n_c = \int_{E_G}^{\infty} N_c(E)F(E)dE \tag{13}$$

$$n_{l\hbar} = \int_{o}^{-\infty} N_{\hbar l}(E)F(E)dE \tag{14}$$

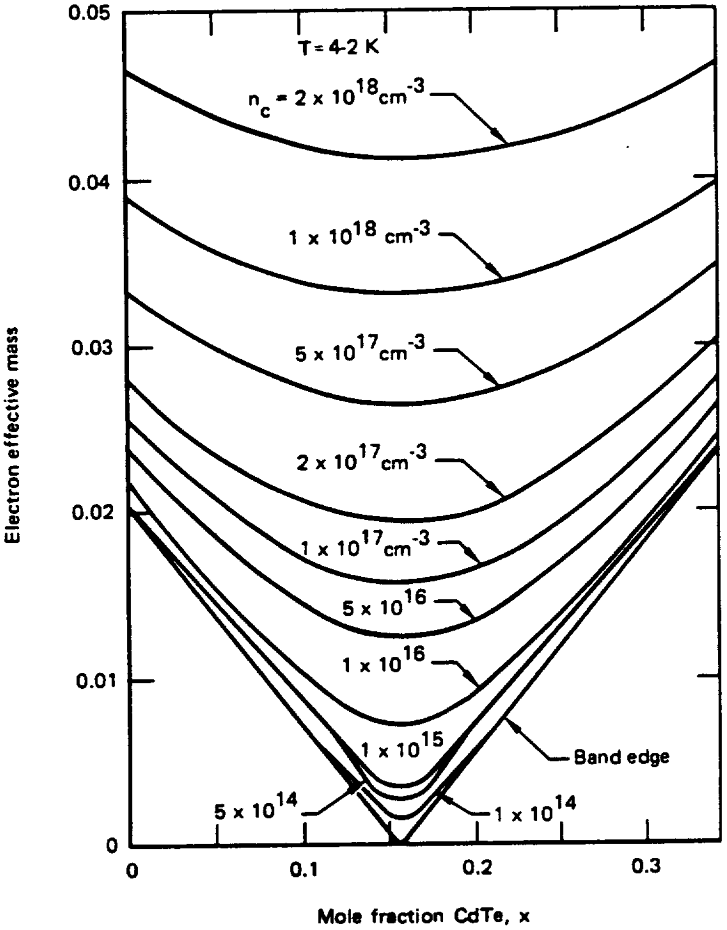

Figure 2. Dependence of conduction band electron effective mass on mole fraction of Cd in low x-valued $Hg_{1-x}Cd_xTe$ alloys.

$$n_{hh} = \int_{o}^{-\infty} N_{hh}(E)F(E)dE \qquad (15)$$

where $N_C(E)$, $N_{lh}(E)$ and $N_{hh}(E)$ are the density of states for the conduction band, light-hole and heavy-hole valence bands, respectivity. F(E) is the Fermi-Dirac Function:

$$F(E) = (1 + e^{(E-E_f)}/kT)^{-1} \qquad (16)$$

in which $E_F$ is the Fermi level.

Values for $E_F$, and $n_c$, $n_{lh}$ and $n_{hh}$ are obtained from the numerical solution of the charge neutrality equation;

$$n_c - n_{lh} - n_{hh} = N_D - N_A \qquad (17)$$

The values obtained for the intrinsic carrier concentration ($N_D = N_A = 0$) as a function of temperature are plotted in Figure 3 for alloys with $E_G \approx 5$, 10, 15 and 20 $\mu$m. The intrinsic electron concentration, $n_i$, decreases rapidly with decreasing temperature and/or increasing energy-gap in the manner shown in the figure.

Reasonable agreement is obtained with experiment and an empirical equation derived by Hansen and Schmitt[8]

$$n_i = (5.585 - 3.82x + 1.753 \times 10^{-3}\, T - 1.364 \times 10^{-3}\, x\, T \qquad (18)$$

$$\times\ [1 \times 10^{14}\, E_G^{3/4}\, T^{3/2} \exp(-E_G/2kT)\ ]$$

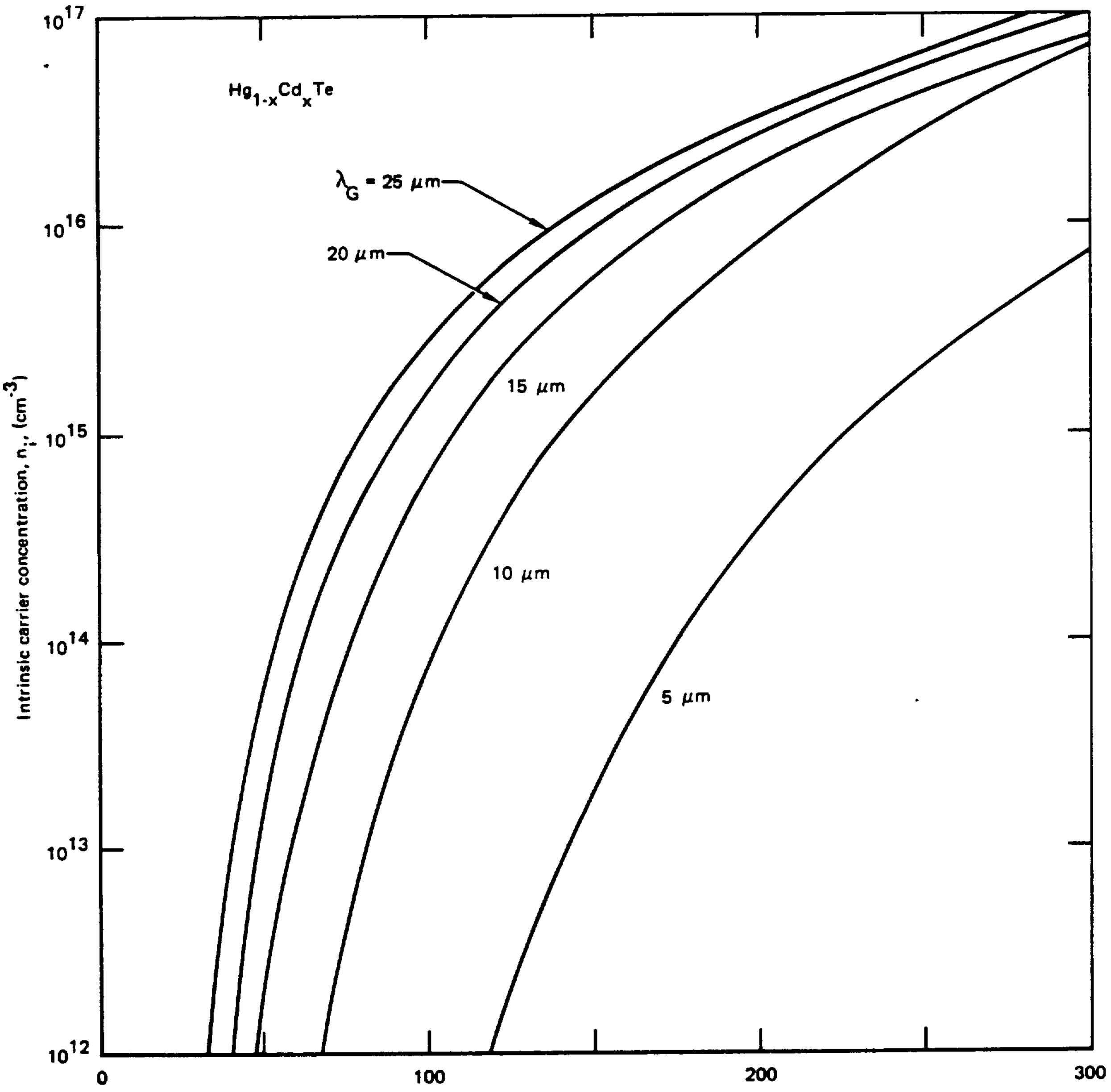

Figure 3. Dependence on intrinsic carrier concentration on temperature for HgCdTe alloys with bandgap energies corresponding to 5, 10, 15 and 20 μm.

In a doped semiconductor the majority and minority carrier concentrations are related by the expression

$$pn = n_i^2 \tag{20}$$

### 2.1.2 Carrier Mobilities

The behavior of the electron mobility in HgCdTe alloys is reasonable well understood as demonstrated by Figure 4 where the temperature dependence of the mobility measured for a sample with x = 0.193 is well fitted by theory. The theory calculates the limit imposed on the electron mobility, $\mu_T$ from scattering by longitudinal optical phonons, $\mu_{LO}$, longitudinal and acoustic phonons, $\mu_{ac}$, ionized impurities $\mu_{ii}$, heavy holes, $\mu_{hh}$, and the compositional disorder potential of the alloy, $\mu_{dis}$, whose individual contributions are also plotted in Figure 4.[9] It is shown that acoustic phonon scattering is negligible at all temperatures and alloy compositions and that above 70K the mobility is limited principally by LO scattering with significant contributions coming from alloy disorder and heavy-hole scattering above 120K. For temperatures below 50K ionized impurity scattering becomes increasingly important and completely dominates the mobility below 20K. Similar results to those shown in Figure 4 have been obtained by Scott[10] for alloy compositions between 0.0 and 0.70. From theoretical fits to low-temperature mobility data quite accurate

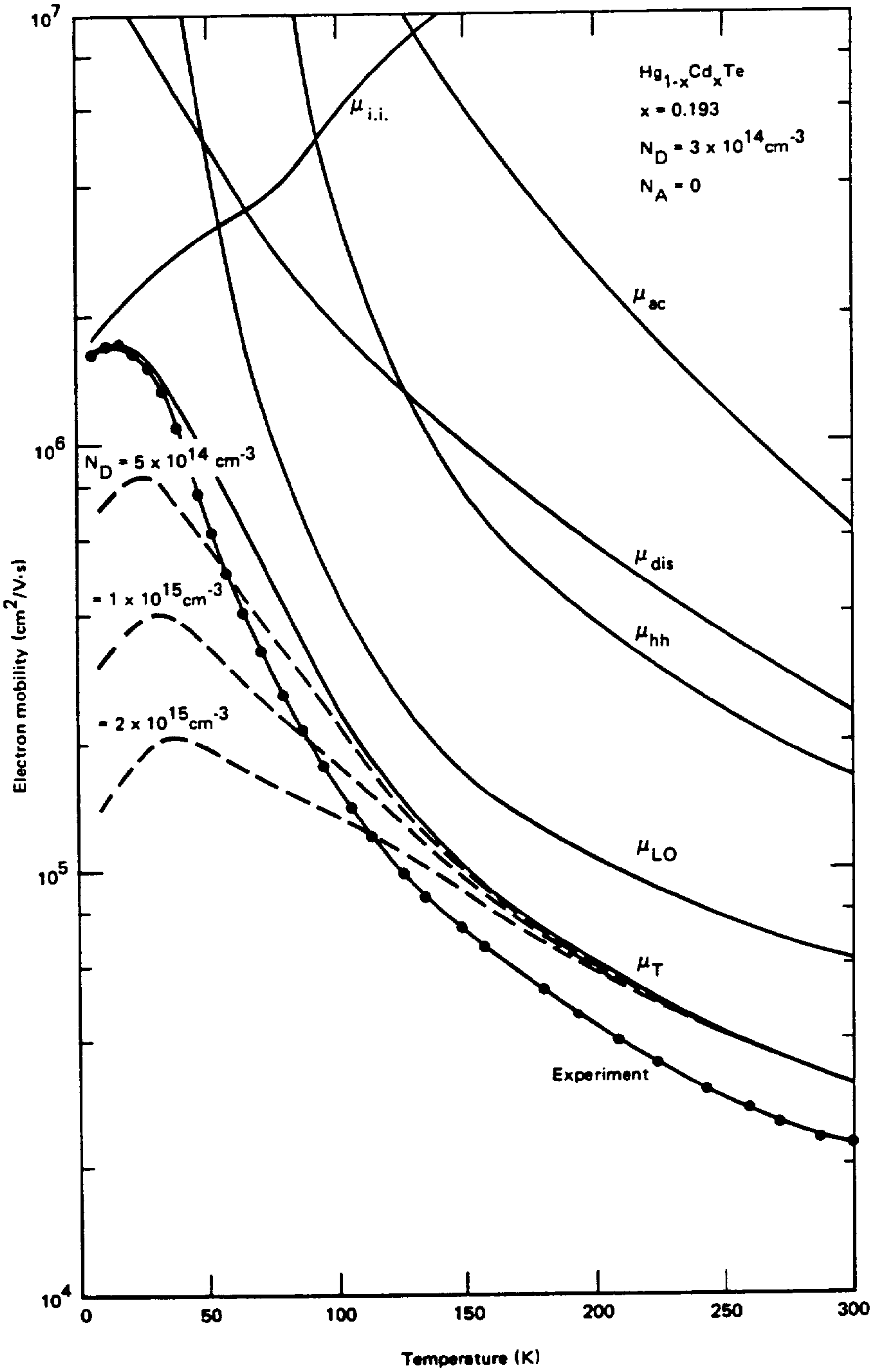

Figure 4. Temperature dependence of electron mobility in a HgCdTe alloy with x = 0.193[9].

estimates can be obtained of the acceptor concentrations and, therefore, sample compensation. Generally 77K mobility values greater than $2 \times 10^5$ cm$^2$/V·s are an indication of good quality material, although for quantitative estimates lower temperature measurements are required.

There have been few measurements of hole mobilities in HgCdTe and no extensive theoretically studies. Values measured at 77K range between 50-500 cm$^2$/V·s and are more than an order of magnitude less than theoretical estimates and values reported for p-type III-V compounds.

An important parameter associated with carrier mobility is the carrier diffusion coefficient D, which in thermal equilibrium is related to the drift mobility by the expression

$$D_{n,\,p} = 2\left(\frac{k^{T}}{8}\,\mu_{n,\,p}\right)\frac{F_{1/2}\left(\frac{E_c - E_F}{kT}\right)}{F_{-1/2}\left(\frac{E_c - E_F}{kT}\right)} \qquad (21)$$

For a non-degenerate semiconductor, the above equation reduces to the Einstein relationship,

$$D_{n,\,p} = \left(\frac{kT}{q}\right)\mu_{n,\,p} \qquad (22)$$

### 2.1.3 Carrier Diffusion Lengths

This parameter can be measured experimentally, which is important in device design considerations. It measures the average distance traveled by an excess-carrier during its lifetime and is given by the expressions

$$L_{n,\,p} = (D_{n,\,p}\tau_{n,\,p})^{1/2} \tag{23}$$

In a pure crystal, $D_n > D_p$ because $\mu_n > \mu_p$, and $\tau_n = \tau_p$. Thus $L_n > L_p$.

To date the experimental determinations of $L_n$ or $L_p$ have been few and limited to p-type material. Values of ~ 120$\mu$m are reported for x = 0.38 and p = 5 x $10^{15}$ cm$^{-3}$ at 77K.

### 2.1.4 Carrier Recombination Mechanisms.

The intrinsic recombination mechanisms that have been identified to date as imposing a fundamental limit on electron and hole lifetimes in n- and p-type HgCdTe alloys are shown schematically in Figure 5 and are described briefly below. Beattie[11] has numbered thirteen possible Auger recombinations transitions in direct bandgap semiconductors and his tabulation scheme is used here.

(a) Radiative Recombination: Electron-hole pairs recombine with the simultaneous emission of a photon of energy $h\nu$[12]. This process occurs in both n- and p-type material and is strongly dependent on $E_G$, T and the majority carrier concentration. The radiative recombination rate, $U_R$, and lifetime, $\tau_R$, are given by the expression

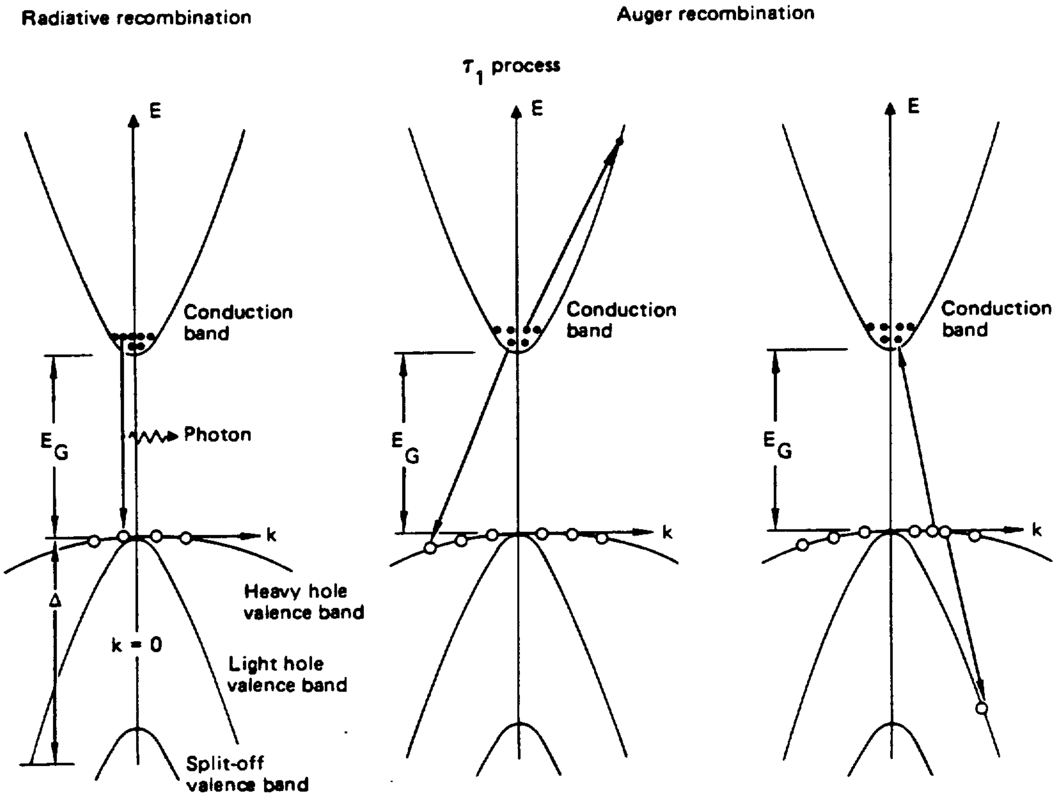

Figure 5. Intrinsic recombination processes in HgCdTe.

$$\tau_R = \frac{\Delta n}{U_R} \ , \quad \text{where} \quad U_R = B_R(np - n_i^2) \tag{24}$$

and $\Delta n = \Delta p$ is the excess photon excited carrier concentration.

For a non-degenerate semiconductor with parabolic energy bands,

$$B_R = \frac{5.8 \times 10^{-13}\, \epsilon_\infty^{1/2}}{(m_e + m_{hh})^{3/2}} \bullet \left(1.0 + \frac{1}{m_e} + \frac{1}{m_{hh}}\right)\left(\frac{300}{T}\right)^{3/2} E_G^2 \tag{25}$$

(b) <u>The Auger 1 Process</u>: Two electrons collide such that one electron drops into an empty valence band state (hole) and imparts its recombination energy to the second electron which is thereby excited to a higher empty state in the conduction band[13]. The Auger 1 lifetime, $\tau_{A1}$, and recombination rate, $U_{A1}$, are strongly dependent on $E_G$, T and $n_c^2$, and are given by the expressions

$$\tau_{A1} = \frac{\Delta n}{U_{A1}} \ ; \quad \text{where} \quad U_{A1} = B_1\, n(np - n_i^2) \tag{26}$$

and for a non-degenerate semiconductor with parabolic energy bands;

$$B_1 = 1.32 \times 10^{17} \frac{m_e F_1^2}{\varepsilon_\infty^2 + (1 + m_u)(1 + 2m_\mu)} \left(\frac{kT}{E_G}\right)^{3/2} \exp\left(-\left(\frac{1 + 2m_\mu}{1 + m_\mu}\right)\frac{E_G}{kT}\right) \tag{27}$$

where

$$m_\mu = m_e/m_{hh}$$

(c) <u>The Auger 7 Process</u>: Two heavy-holes collide and are scattered into final states in the conduction band and light-hole band respectively[14]. This is a three-band mechanism which was first proposed for InSb.[15] It has also been suggested as a possible lifetime limiting mechanism in p-type HgCdTe.[14] It has been estimated that the scattering probability of this mechanism is approximately 1/10 of the Auger 1 mechanism. Thus the Auger 7 lifetime, $\tau_{A7}$, and recombination rate, $U_{A7}$, are given by:

$$\tau_{A7} = \frac{\Delta n}{U_{A7}} \text{ ; where } U_{A7} = B_7 p(np - n_i^2) \tag{27}$$

and

$$B_7 = B_1/10. \tag{28}$$

From equations, 23 - 28 the total carrier lifetime from intrinsic processes was calculated from the expression

$$\frac{1}{\tau_T} = \frac{1}{\tau_R} + \frac{1}{\tau_{A1}} + \frac{1}{\tau_{A7}} \qquad (29)$$

To determine the relative magnitudes of these processes the temperature dependence of $\tau_R$, $\tau_{A1}$ , and $\tau_{A7}$ has been calculated for electron and hole concentrations between 3 x $10^{16}$ and 1 x $10^{14}$ $cm^{-3}$. The results of these computations for alloys with constant band gap energies corresponding to 5, 10 and 15 μm is shown in Figures 6, 7, and 8, respectively.

In these figures all of the intrinsic recombination lifetimes are observed to decrease rapidly with increasing temperature and decreasing band gap energy. This is a direct consequence of the behavior of the intrinsic carrier concentration, (Figure 3) and because all of the recombination coefficients also decrease with decreasing temperature and bandgap energy. For equal carrier densities the radiative lifetime is the same for both n- and p-type alloys, whereas the Auger 1 is the dominant Auger process in all n-type alloys and p-type alloys with hole concentrations

$$p < \frac{B_1}{B_7} n \qquad (30)$$

For higher hole concentrations the Auger 7 process becomes the dominant Auger recombination mechanism and provides a possible alternative recombination path to the radiative process, which until recently had been considered to be the only recombination

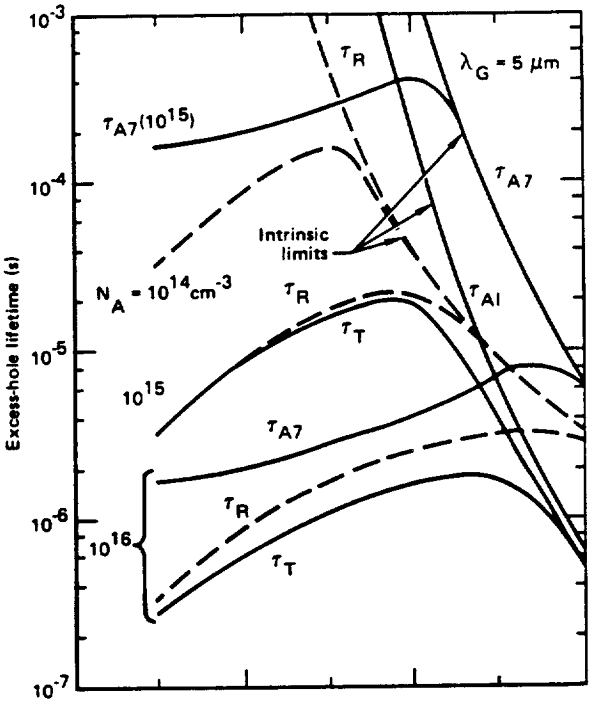

Figure 6. Excess-hole lifetime as a function of temperature for a HgCdTe alloy with a bandgap energy corresponding to $5\mu m$.

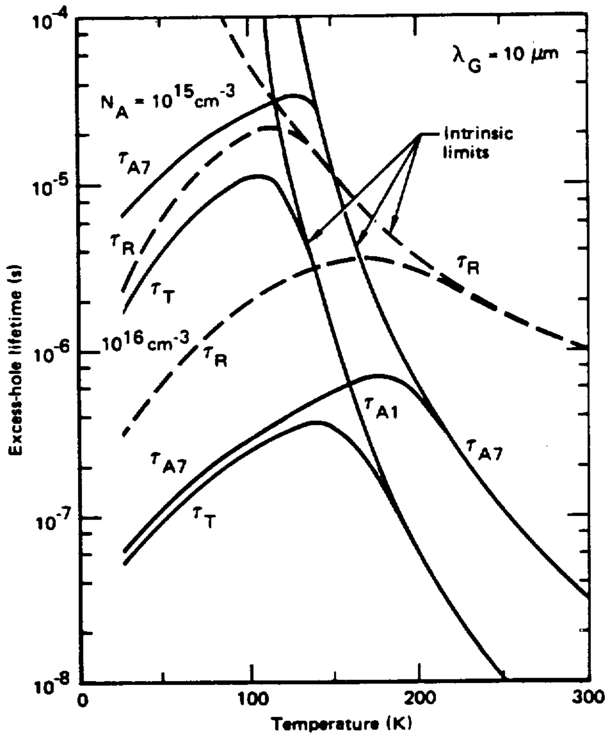

Figure 7. Excess hole lifetime as a function of temperature for a HgCdTe alloy with a bandgap energy corresponding to 10 $\mu m$.

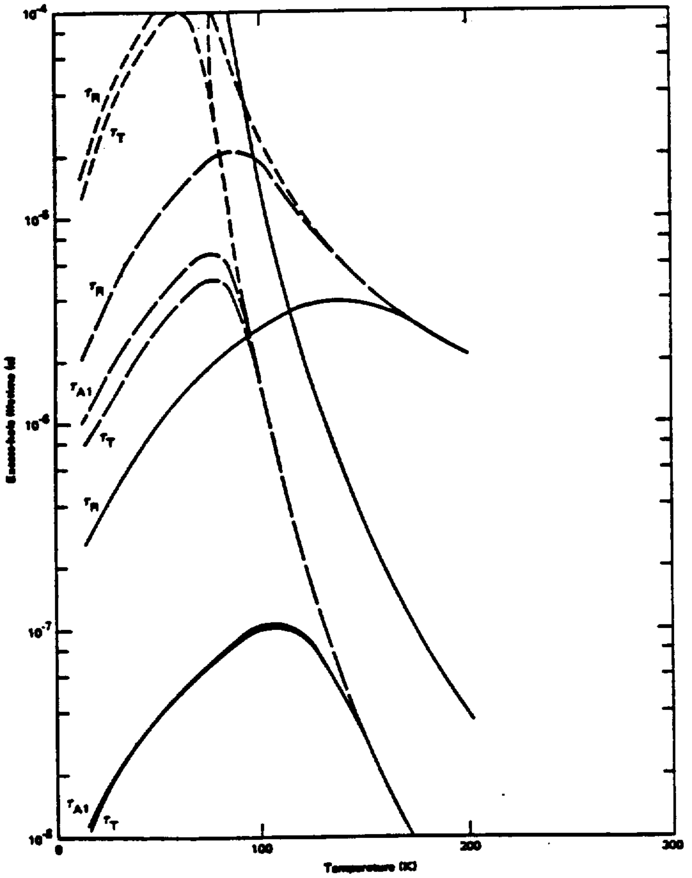

Figure 8. Dependence of excess-hole lifetime on temperature for a HgCdTe alloy with a bandgap energy corresponding to 15 $\mu$m.

mechanism in p-type material.

Figure 6 shows that for 5 $\mu$m intrinsic HgCdTe the hole lifetime is limited by radiative recombination below 240K and by electron-electron collisions (the Auger 1 process) above 240K. For hole concentrations < $10^{15}$ cm$^{-3}$ the radiative process dominates below 200K. However, for hole concentrations > $10^{16}$ cm$^{-3}$ the Auger 7 process involving heavy-hole-heavy-hole collisions, dominates the lifetime characteristics. For hole concentrations less than $10^{15}$ cm$^{-3}$ hole lifetimes longer than $10^{-5}$s are predicted between 100-220K.

For 10 $\mu$m HgCdTe the same general temperature dependences are observed, however the intrinsic limits on the hole lifetimes have moved to significantly lower temperatures, the radiative process becoming dominate below 115 K. The Auger 7 and radiative recombination rates are now comparable for hole concentration of $10^{15}$ cm$^{-3}$ and the Auger 7 process completely dominates for hole concentrations higher than $10^{16}$ cm$^{-3}$. To achieve hole lifetimes > $10^{-5}$s, hole concentrations < 5 x $10^{14}$ cm$^{-3}$ and operating temperatures below 100K are required. For 15 $\mu$m the same trend is observed; the Auger 7 process dominates for hole concentrations > $10^{14}$ cm$^{-3}$ and temperatures > 70K.

For HgCdTe alloys with energy gaps equal to or longer than 10 $\mu$m the Auger 7 process is shown to have a significant effect on the hole lifetime between 300-10K and thus on the ultimate achievable device performance.

## 2.2 Optimum Device Geometry

To optimize the efficiency of a long-wavelength terrestrial power cell it is necessary to capture all of the incident photon flux so as to create an electron-hole distribution that is completely collected by the junction, and also, to minimize all device currents with respect to the photon generated current. Thus the size and type of device structure required to optimize the power conversion efficiency is determined by the mechanisms of photon capture and the transport properties of the photon-excited electron-hole plasma. The important material parameters are therefore the absorption coefficient and carrier diffusion lengths. To obtain photon capture coefficients with efficiencies > 90% the active optoelectronic region of the device must have a thickness approximately equal to $2/\alpha$, and for all of these carriers to be collected either $L_n$ and $L_p$ (the electron hole and diffusion lengths) must be greater than $2/\alpha$. Calculations of the absorption coefficient, $\alpha$, and $L_n$ and $L_p$ for the HgCdTe alloy systems are given in Table 1 and show that these parameters decrease with energy gap. The estimates for the diffusion lengths were calculated using the expressions given previously for a temperature of 77K and carrier concentrations of $10^{14}$, $5 \times 10^{14}$ and $1 \times 10^{15}$ cm$^{-3}$. In this estimate the values of $\mu_n = 10^4$ cm$^2$/V·s and $\mu_p = 500$ cm$^2$/V·s were used.

Table 1 shows that because $\mu_n > \mu_p$ and $\tau_n$ is generally $> \tau_p$, $L_n$ is always greater than $L_p$. Thus for long wavelength applications, the condition that $L_n$, $L_p > 2/\alpha$ for all electron-hole pairs to reach

**Table 1.** Absorption coefficients and carrier diffusion lengths at 77 K for $Hg_{1-x}Cd_xTe$ alloys with band-gap energies corresponding to 5, 10 and 15 $\mu$m and $N_A = N_D = 10^{15}$ $cm^{-3}$.

| Cutoff wavelength, $\lambda_g$ ($\mu$m) | Absorption coefficient, $\alpha$ ($cm^{-1}$) | $2/\alpha$ ($\mu$m) | Diffusion length for electrons in p-type region, $L_n$ ($\mu$m) | Diffusion length for holes in n-type region, $L_p$ ($\mu$m) |
|---|---|---|---|---|
| 5 | $4 \times 10^3$ | 5 | 198 | 27 |
| 10 | $10^3$ | 20 | 52 | 11 |
| 15 | $4 \times 10^2$ | 50 | 19 | 7 |

the junction is more likely to be satisfied for p-type HgCdTe. The most effective device structure for the power conversion of infrared radiation is, therefore, the $n^+$ on p structure, which can be fabricated by ion-implantation of p-type HgCdTe wafers or grown by molecular beam epitaxy. By making the $n^+$ region thin ($< 0.5\ \mu m$) and more heavily doped than the p-type region, all incident radiation will be absorbed in the p-type region which is predicted to have superior photoconductive properties.

Table 1 also shows that hole concentrations of $10^{14}$ $cm^{-3}$ or less are required to maximize the collection of charge carriers in long-wavelength diode structures.

## 2.3 Junction Theory

The intrinsic processes giving rise to charge-carrier transport across a p-n junction have been discussed by Sze,[16] Sah[17] and Evans and Landsberg[18] and are shown schematically in Figure 9. The principal mechanisms are the diffusion of minority carriers across the depletion layer, carrier generation and recombination within the depletion layer, and the tunneling of carriers through the depletion region. Because of the wide range of energy gaps and temperatures for which HgCdTe alloys may be used as power cells it is possible for each process to dominate for some conditions of operation of the device. Therefore all of the mechanisms were included in the calculations.

The barrier voltage $V_b$ and the junction width W of the diode

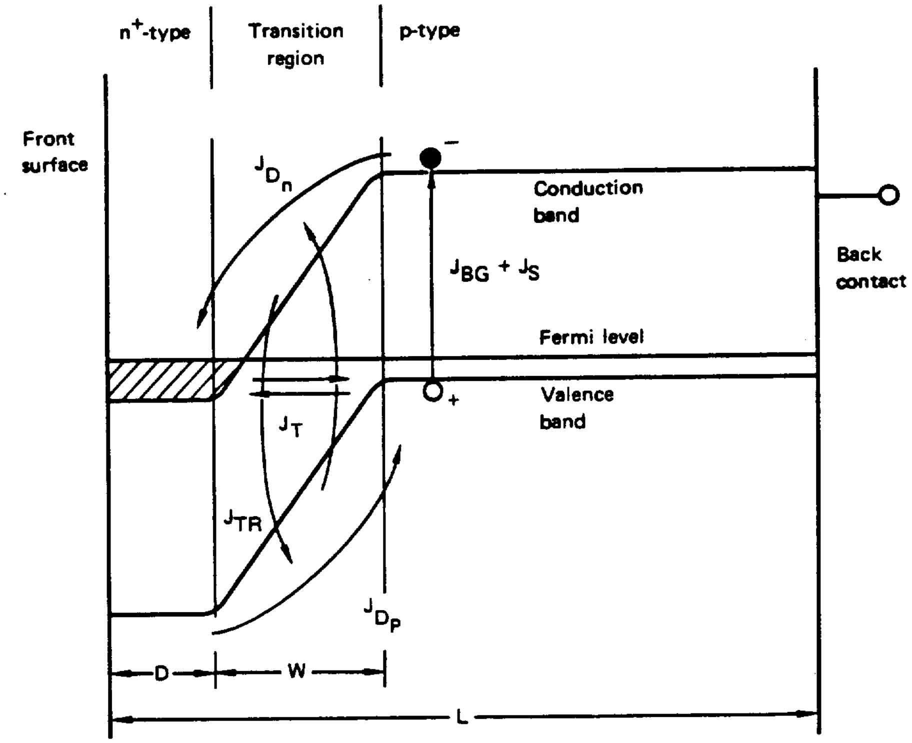

Figure 9. Schematic of charge-carrier transport across a p-n junction.

were obtained from the expressions,

$$V_b = \frac{kT}{e} \ln\left(\frac{n_{po}\, p_{po}}{n_i^2}\right) \tag{31}$$

and,

$$W = \left(\frac{2\varepsilon_S\, \varepsilon_O(V_b - V)\; n_{po}\, p_{po}}{qn_{no}\, p_{po}}\right)^{1/2}, \tag{32}$$

where $n_i$ is the intrinsic carrier concentration, $n_{po}$ and $p_{po}$ are the equilibrium electron and hole concentrations in the p-type layer, $n_{no}$ and $p_{no}$ are the equilibrium electron and hole concentrations in the n-type layer, $\epsilon_S$ is the dielectric constant of the semiconductor, $\epsilon_0$ is the permittivity of free space, k is Boltzmann's constant, q is the electronic charge, T is the temperature, and V is the applied voltage.

The diffusion current, $J_D$, was calculated from the expression

$$J_D = J_{Dn} + J_{Dp}, \tag{33}$$

where $J_{Dn}$ and $J_{Dp}$, the diffusion currents associated with minority carriers on the p- and n-side of the junction, respectively, and are given by the expressions

$$J_{Dn} = \frac{eL_n n_{po}}{\tau_n}\left(e^{\beta} - 1\right) \quad \text{and} \quad J_{Dp} = -\frac{eL_p\, p_{no}}{\tau_p}\left(e^{\beta} - 1\right), \tag{34}$$

where $\beta$ = qV/kT, and $\tau_n$ and $\tau_p$ are the lifetime times of minority carriers (electron and holes) on the p- and n-side of the junction, respectively. Thus for an $n^+$-p structure, $J_{Dn} >> J_{Dp}$, and the diffusion current is controlled by the flow of minority carriers (electrons) from the p side to the n side of the junction.

The current produced in the transition region, $J_{TR}$, by the generation and recombination of charge carriers is given by

$$J_{TR} = e \int_{-W/2}^{W/2} (B_R + nB_1 + pB_7)\ (np - n_i^2)dx, \qquad (35)$$

which for intrinsic recombination processes reduces to the expression first obtained by Evans and Landsberg for a nondegenerate semiconductor.

$$J_{TR} = en_i^2\ WB_R + (n_{po}\ B_1 + p_{po}\ B_7)$$

$$(36)$$

$$\times \left( \frac{\exp\ [1/2(\beta_b - \beta)] + \exp\ [-1/2(\beta_b - \beta]}{1/2(\beta_b - \beta)} \right) \exp \left[1/2(\beta_b + \beta)\right] ,$$

where

$$\beta_b = eV_b/(kT)$$

The tunnel current, $J_T$, was calculated from the following expression derived for a degenerate semiconductor with a parabolic band structure[19]:

$$J_T = C_1 \, (V - V_b) \, \exp\left[- C_2 (V - V_b)^{1/2}\right] , \qquad (37)$$

where

$$C_1 = \frac{3e^2}{8\pi^3 h^2} \left\{ \frac{m^*}{\varepsilon_o \varepsilon_s \varepsilon_G} \, \frac{n_{no} p_{po}}{n_{no} + p_{po}} \right\}^{1/2}$$

and

$$C_2 = \frac{\pi E_G}{3\hbar} \left\{ \frac{m^* E_G \varepsilon_o \varepsilon_s (n_{no} + p_{po})}{n_{no} \, p_{po}} \right\} ,$$

In the above expression, $m^*$ is the effective mass of electrons tunneling through the junction. The total dark current flow in an ideal n-p junction structure is given by the expression.

$$J_{DK} = J_D + J_{TR} + J_T \, . \qquad (38)$$

The current density delivered to the load is then the difference of the current density due to absorbed radiation from the source and thermal background and the equivalent current density of the radiation re-emitted from the top surface of the cell or absorbed in the substrate. Thus the total device current is:

$$J = J_{ph} + J_{th} - J_{rad} - J_D - J_{TR} - J_T \qquad (39)$$

where $J_{ph}$, $J_{th}$, $J_{rad}$, $J_D$ and $J_{TR}$ are the photon induced current the thermal induced current, the radiatively remitted current, the device diffusion current and the generation-recombination current, respectively.

## 2.4 Calculation for Homojunction Power Cell Efficiency

To estimate the ideal performance of a terrestrial power cell ($J_{Dk}$ = 0) we apply the scheme used by Henry[1] to calculate the limiting efficiencies of ideal single and multiple energy gap terrestrial solar cells. This approach calculates the efficiency by only considering the two intrinsic loss mechanisms which limit the efficiency of an ideal solar energy cell. The first intrinsic loss mechanism is the inability of a single energy gap cell to properly match a broad spectrum. Photons with energies $h\nu$, less than the bandgap energy, $E_G$, are not absorbed and photons with $h\nu > E_G$ generate electron-hole paris which very rapidly lose most of their energy in excess of $E_G$ to optical phonon scattering. The second major loss is due to radiative recombination by the cell. The rate of radiative emission increases exponentially with the applied bias energy eV, were V is the voltage developed across the load.

The many extrinsic limitations that are not considered in this calculation include losses due to reflection, contacts, series resistance, absorption in window layers, incomplete photon collection, nonradiative recombination and cell heating.

To avoid excessive complications the calculation is performed for a 300 K blackbody spectrum. Thus the photon flux $\delta n_{ph}(E)/\delta E$(in photons $cm^{-2}s^{-1}/eV$) is calculated as a function of bandgap energy, $E_G$, using the formula

$$\frac{\delta n_{ph}}{\delta E}(E_G) = \frac{2\pi\nu c^2}{e^{h\nu/kT}-1} \quad . \tag{40}$$

Here it is assumed that the semiconductor is opaque for photons with energies greater than $E_G$, and transparent for photons with energies less than $E_G$. Consequently the number of photons absorbed by a semiconductor with bandgap $E_G$ is given by integrating Equation 40 for all energies above $E_G$; i.e.

$$n_{ph}(E_G) = \int_{E_G}^{\infty} \frac{dn_{ph}}{dE} \cdot dE \tag{41}$$

The area under the $n_{ph}(E_G)$ vs. $E_G$ curve is therefore equal to the total cell power generated per unit area, i.e.

$$P = \int_{o}^{\infty} n_{ph} \bullet dE_G \tag{42}$$

To be able to calculate the efficiency of an energy cell it is first necessary to determine the maximum work that can be done by each absorbed photon. The total current density, J, delivered to the load of the cell is the sum of the current densities produced by the photon flux ($J_{ph}$) and ambient thermal radiation ($J_{the}$), minus the current density ($J_{rad}$) lost by radiative recombination from the top and bottom surfaces the cell. Thus from Equation 39,

$$J = J_{ph} + J_{th} - J_{rad} \tag{43}$$

where

$$J_{ph} = en_{ph} \tag{44}$$

$$J_{th} = A_{th} \exp(-E_G/kT_b) \tag{45}$$

and

$$J_{rad} = A_{rad} \exp((eV - E_G)/kT_B) \tag{46}$$

In these equations

$$A_{rad} = \frac{e(\epsilon_S + 1)E_G^2 kT}{4\pi^2 \hbar^3 c^2} = 407.81 \ \frac{T}{300} \ E_G^2 \ (\epsilon_S + 1) \ \mathrm{A\ cm^{-2}} \tag{47}$$

T is the earths temperature, $T_B$ is the ambient temperature, $E_G$ is the bandgap energy in electron volts, e is the electron charge, k is Boltzman's constant, ħ is Plank's modified constant and c is the velocity of light. Substituting in Equation 43, therefore, gives the total current as:

$$J = en_{ph} + A_{th} \exp\,(-E_G/kT) - A_{rad} \exp((eV - E_G)/kT) \tag{48}$$

The open circuit cell voltage, $V_{oc}$, is then found by setting J = 0.

$$V_{oc} = kT \bullet \ln\left(1 + \frac{qn_{ph}(E_G)}{e^{E_G/kT} - 1}\right) \tag{49}$$

Next the maximum power point, ($J_m$, $V_m$), is found by setting $d(JV)/dV = 0$. This calculation gives

$$eV_m = eV_{oc} - kT\ln\left(1 + \frac{eV_m}{kT}\right) \tag{50}$$

and

$$J_m = \frac{en_{ph}}{1 + kT/eV_m} \tag{51}$$

From these calculations the work done per absorbed photon, W, is obtained from the equation

$$W = \frac{J_m V_m}{n_{ph}} \tag{52}$$

The cell efficiency, $\eta$ is then given by the expression

$$\eta = \frac{100N_{ph}W}{P} \tag{53}$$

where $N_{ph} = n_{ph}(0)$ from Equation 40, and is the total number of photons captured from the earth by the cell.

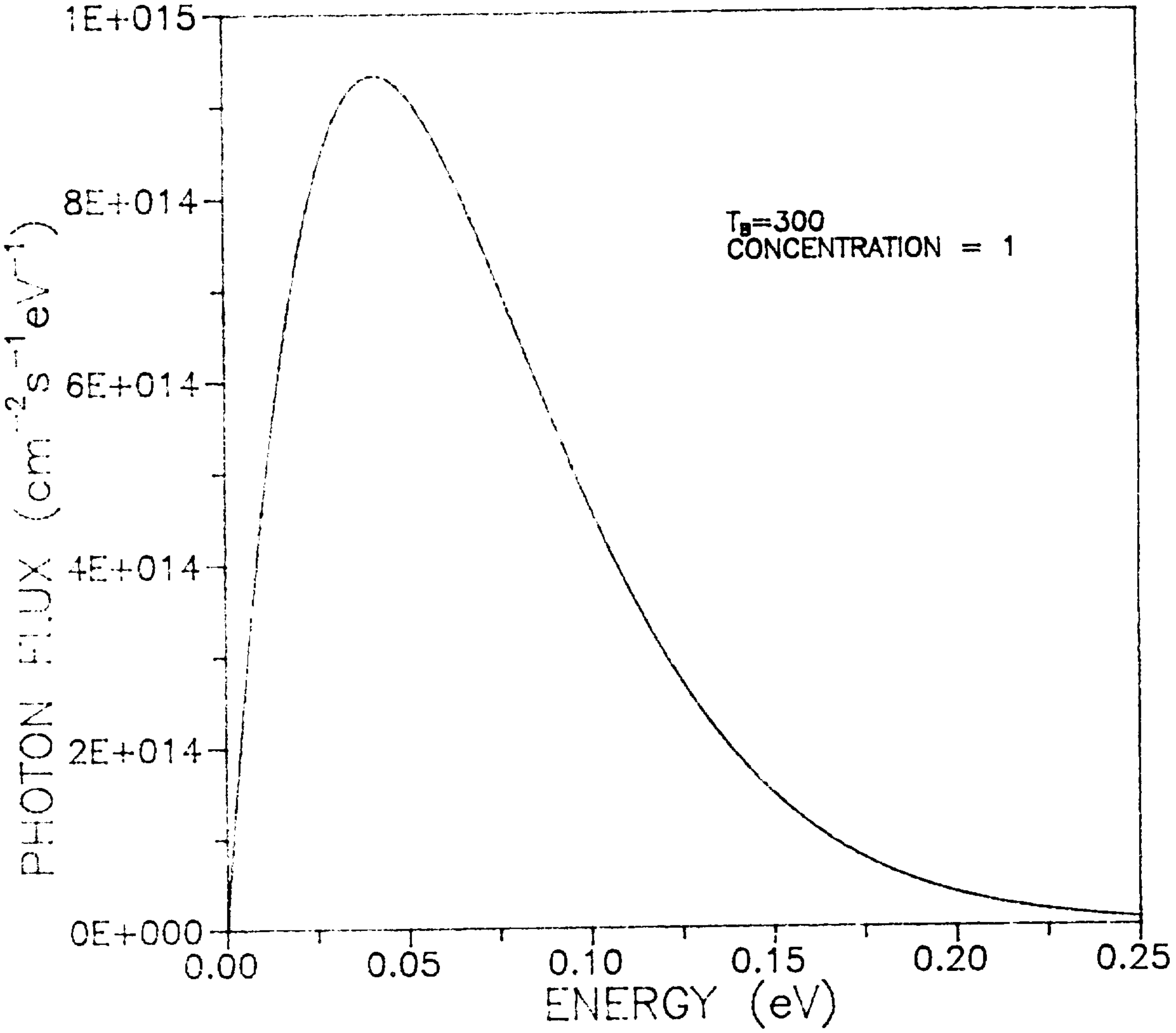

**Figure 10.** Photon concentration as a function of bandgap energy for blackbody at 300K.

### 2.4.1 Numerical Procedure and Results

The numerical calculation used to obtain the cell efficiency as a function of bandgap energy and also photon flux concentration then proceeds as follows. Equation 40 is used to obtain the number of photons emitted as a function of bandgap energy (Figure 10). As shown, this curve peaks at a photon energy of 0.04 eV which corresponds to a wavelength of 31 $\mu$m. From equation 41 the number of photons absorbed by a semiconductor with bandgap energy, $E_G$, is then calculated for $E_G$ values between 0 and 0.25 eV. This curve is labelled the 100% line in Figure 11. The integration of Figure 11 is next performed to obtain the total power per unit area. Finally, for each bandgap energy, solutions are found for $V_{oc}$, $V_m$, $J_m$, and W. The dependence of W on $E_G$ is also shown in Figure 11. As discussed by Henry, Figure 11 can be broken down into four areas. The area labeled $h\nu < E_G$ is identified with photons that are not absorbed and which, therefore, can make no contribution to the power generated by the cell. The area labeled $h\nu > E_G$ is identified with the work lost from photons with energies above $E_G$ which is dissipated as heat in the cell. The area labeled $W < E_G$ is attributed to work lost because of radiative recombination from the cell. Finally the last (unshaded) region equals the power per unit area delivered by the solar cell to the load.

The ratio of this area to the total area under the 100% line gives the efficiency of the cell for one bandgap energy. By calculating this area as a function of energy the dependence of

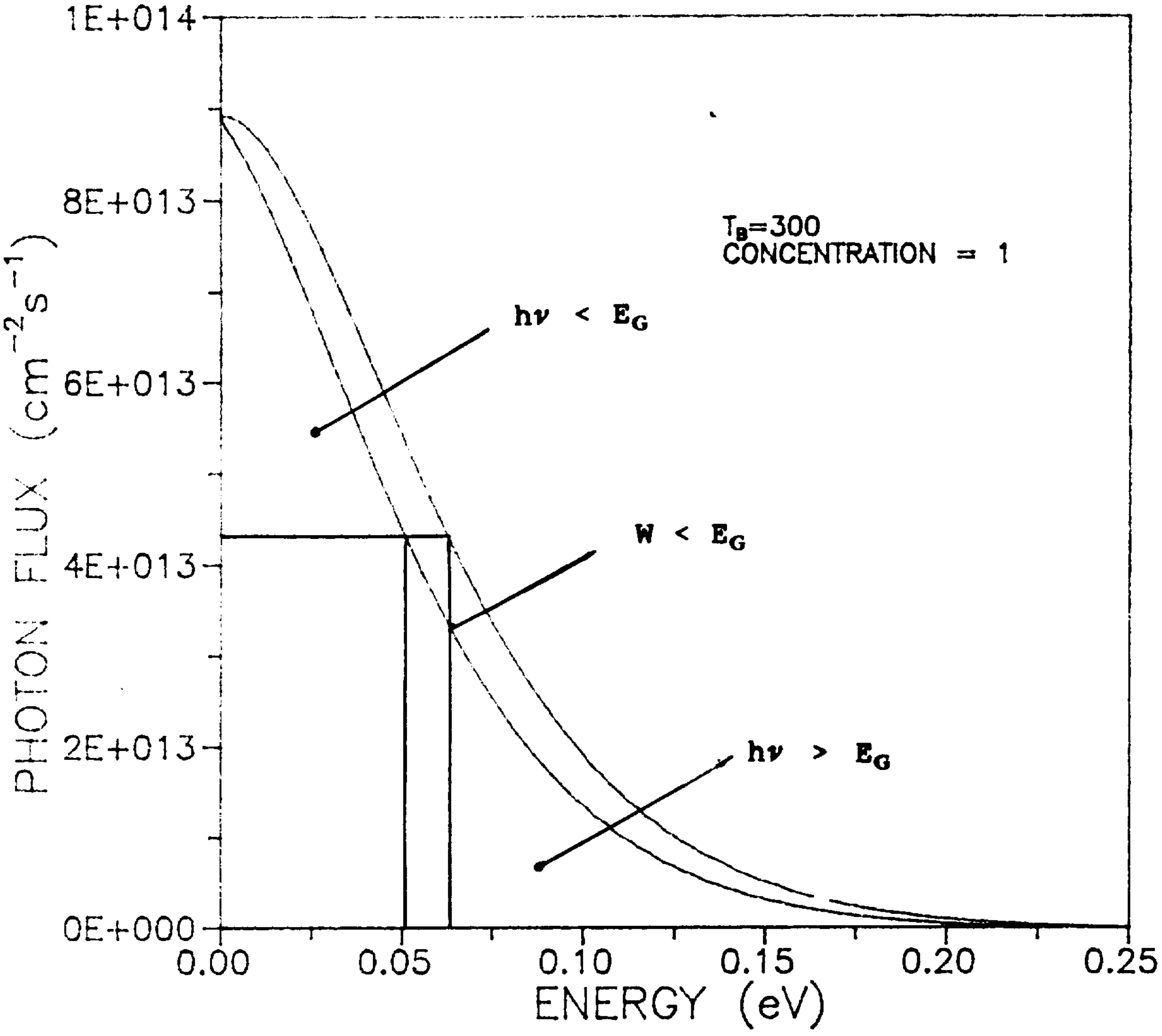

Figure 11. Number of photons in solar spectrum versus photon energy with graphical technique to determine conversion efficiency.

on bandgap energy was obtained as shown in Figure 12. From this curve both of the bandgap energies required to maximize $\eta$ and the value of the peak efficiency is found.

Figure 12 shows the calculation performed for a photon concentration of one and power cell temperature of 10K which is close to the maximum temperature difference possible between the earth's temperature and the temperature of the cell. This calculation indicates a maximum efficiency of 33.7% for a one bandgap cell having an energy gap, $E_G$ = 0.0625 eV.

However, this operating temperature is not very practical for a low earth orbiting satellite for which temperatures between 150-200K are expected, and thus the above calculation was repeated for higher cell temperatures, radiation power concentrators up to 1000, and also multi-bandgap cells.

The repeat of this calculations for cell temperature of 10, 40 and 80k is shown in Figure 13 and indicates that the work done by each photon is reduced very rapidly with increasing power cell temperature. This is because as indicated by Equations 50 and 51 both $V_m$ and $J_m$ decrease in value with increasing temperature. Thus the effective J-V curve softens and less power can be generated by the cell.

Figure 14 shows the maximum possible cell efficiency as a function of the bandgap energy and the temperature of the cell. From the peak of each curve cell efficiencies of 33.7, 11.7 and 1.24 percent are predicted for corresponding bandgap energies of 0.0625, 0.095 and 0.157 eV and temperatures of 10, 40, and 80K,

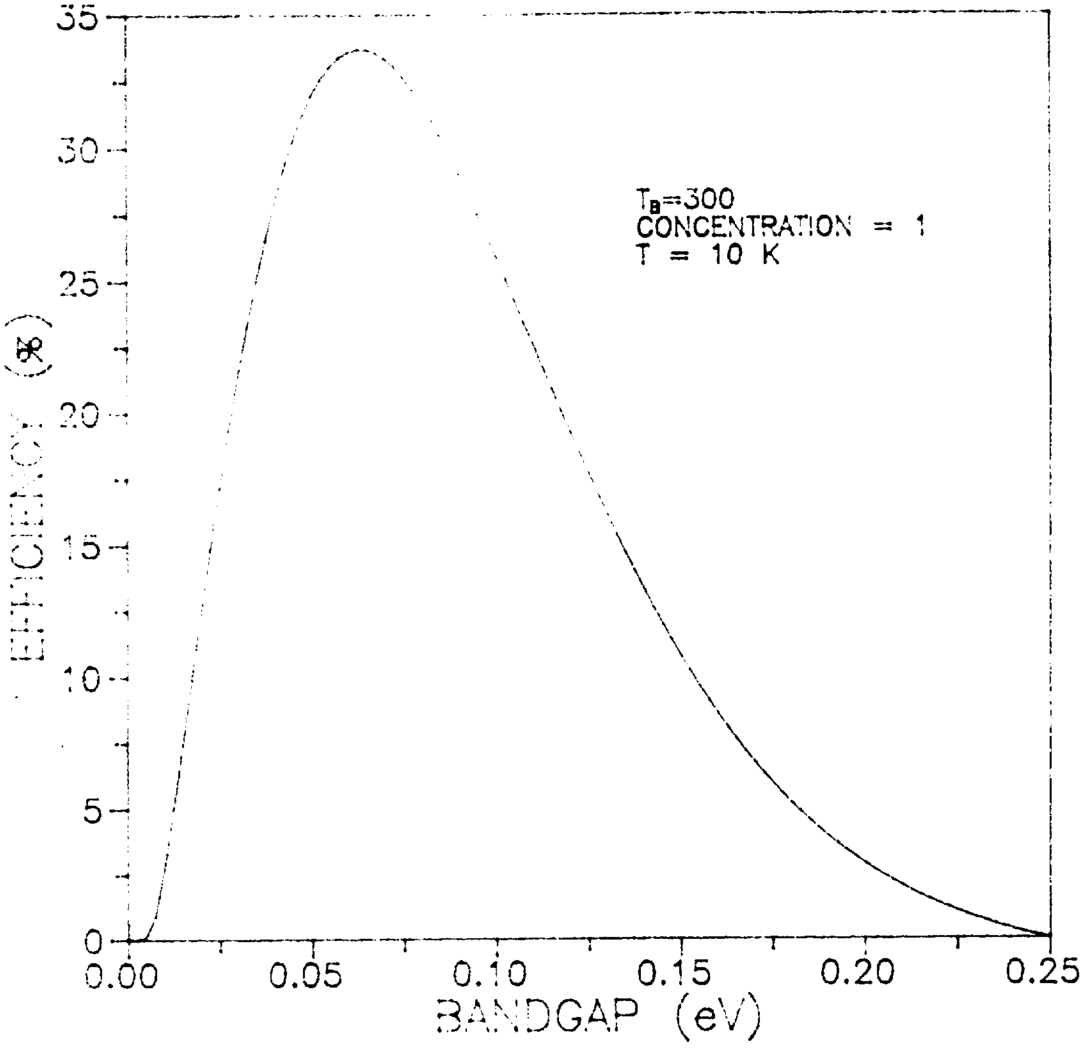

Figure 12. Ideal power cell efficiency at 10K.

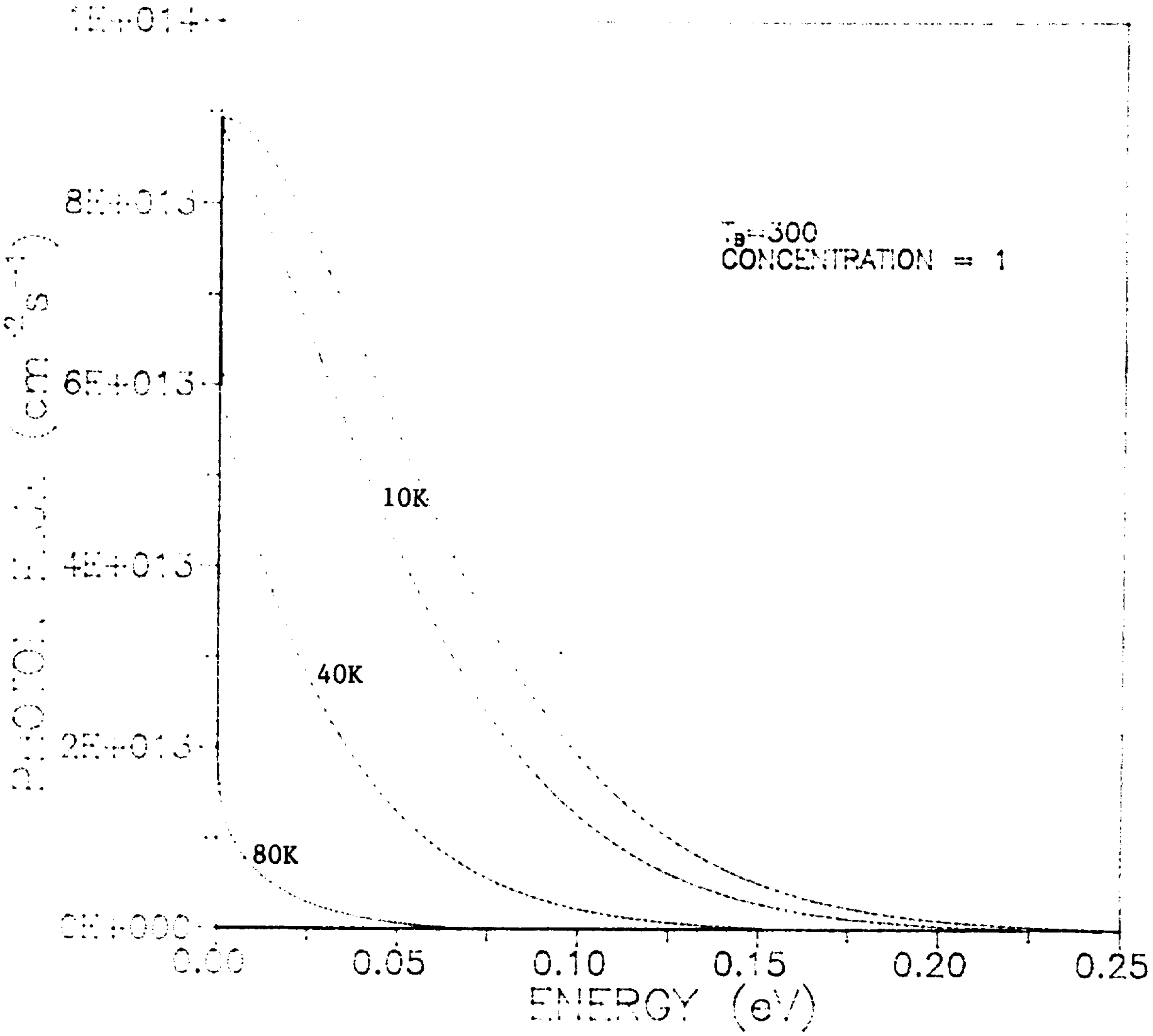

Figure 13. Graphical technique to determine terrestrial power cell efficiency for cell temperature of 10, 40 and 80K.

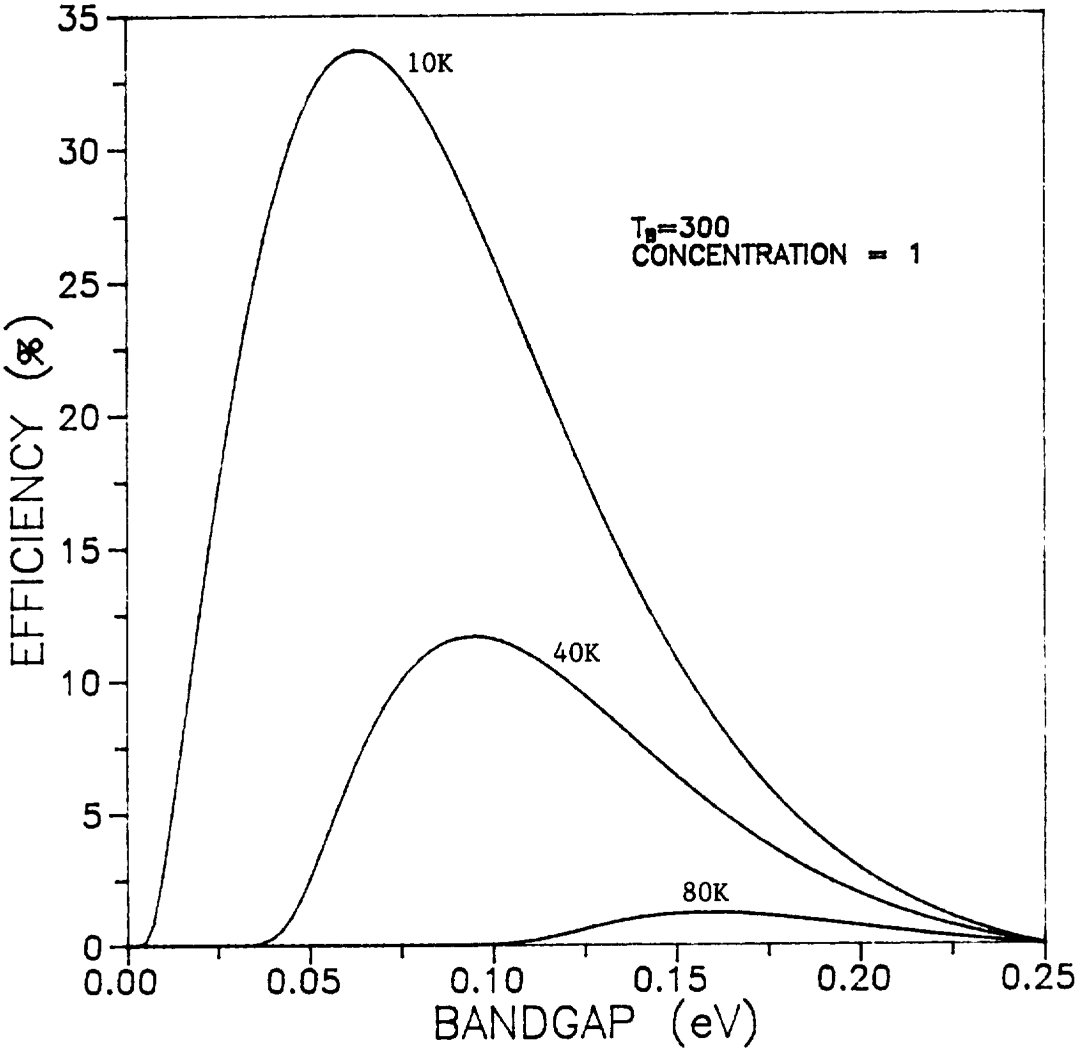

**Figure 14.** Ideal terrestrial power cell efficiency for cell temperatures of 10, 40 and 80K.

respectively. Calculations for higher power cell temperatures indicated that for a single energy bandgap cell the maximum efficiency dropped below 1% above 100K.

Ideally, cell operating temperatures of 150-200K are required as these can be achieved on a satellite without extra cooling. The power consumption needed to cool the power cell array would obviously defeat the purpose of this application. Thus in order to improve cell performance the effect of a radiation power concentrator was next examined for concentration factors up to 1000, the largest possible practical concentration factor. Figure 15 shows the total absorbed photon flux verses the energy bandgap of the cell (outer curve) and the work done per absorbed photon verses the absorbed photon flux for a terrestrial power cell operating with a 1000 times flux concentrator for temperatures of 10, 80, 100 and 150K. As shown the work done per absorbed photon is now significantly higher, principally because of the dependence of $V_{oc}$ on the total collected photon flux. The efficiency vs. bandgap energy for these temperatures and a concentration factor of 1000 are shown in Figure 16. The maximum efficiencies and optimum bandgap energies calculated for a single bandgap cell for these operating conditions are therefore found to be 21.8, 7.53, and 3.62% for bandgap energies of 0.0725, 0.0975 and 0.117 eV at 40, 80, and 100K, respectively. This calculation indicates that for an ideal single bandgap power cell, workable efficiencies of ~ 8% may be achieved for temperatures up to 80K. This situation is demonstrated by Figure 17 in which the maximum cell efficiency for

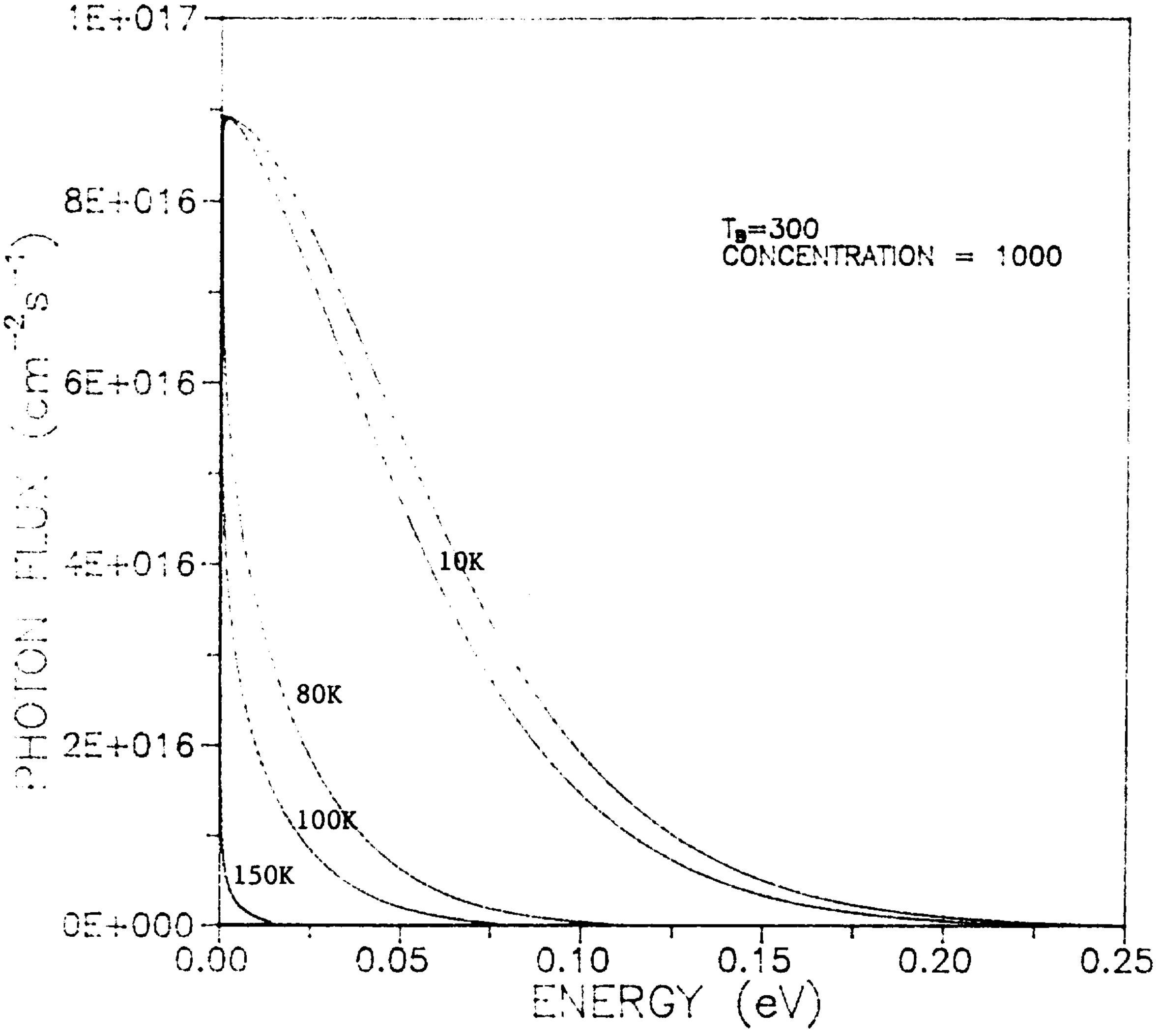

Figure 15. Photon concentration versus energy for terrestrial power cell operating at temperatures of 10, 80, 100 and 150K for 1000 concentration factor.

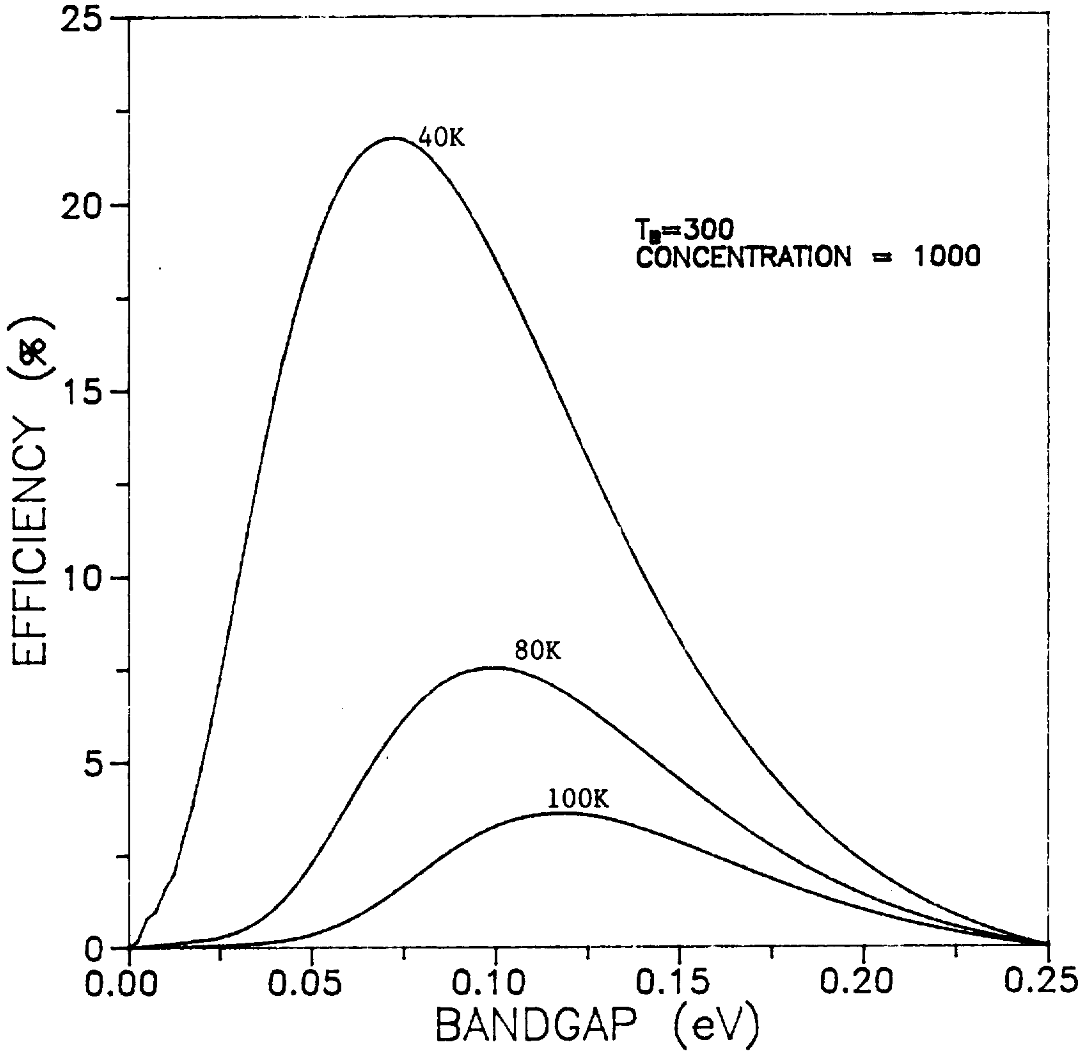

Figure 16. Ideal terrestrial power cell efficiency as a function of bandgap energy for operating temperatures of 40, 80, and 100 at 1000 concentration.

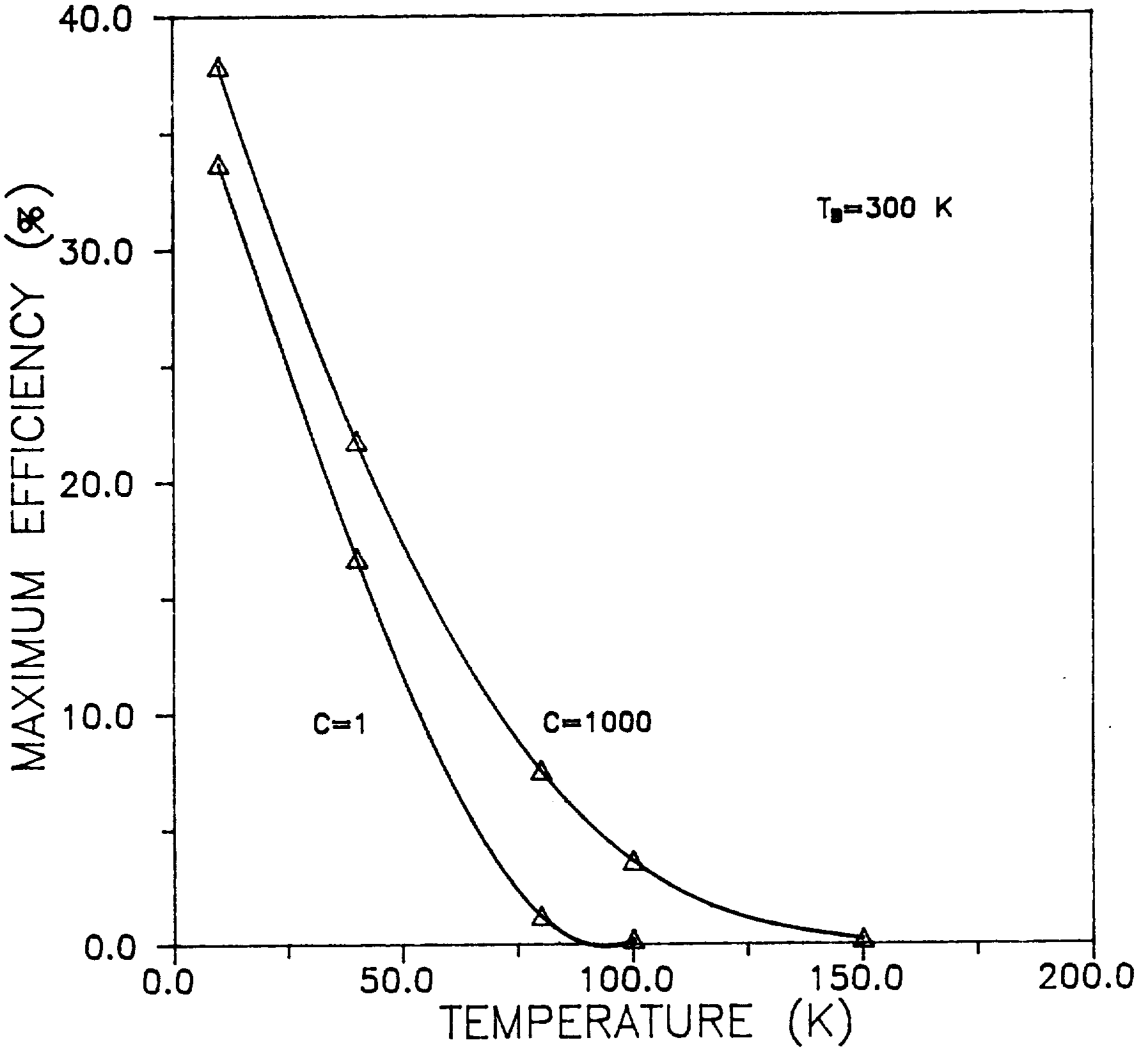

Figure 17. Maximum efficiency for single bandgap power cell as a function of cell temperature for radiation concentration factors of 1 and 1000.

a single bandgap power cell is plotted as a function of cell temperature for radiation concentration factors of one and 1000.

Because it is well know that multi-bandgap cells can provide a better match to the radiation power spectrum, and thus result in enhanced cell efficiencies, the above analysis was extended to this situation for two- and three- bandgap cells. It should be noted that the total power that can be extracted by a multi-bandgap cell having a continuous range of bandgap energies to completely cover the incident power spectrum is given by the area under the W vs. $n_{ph}$, curve divided by the area under the $E_G$ vs. $n_{ph}$ curve.

To perform this calculation the computer program was rewritten to search for all possible cell configurations and to select those with the highest efficiency and to identify the bandgap energies needed to realize this performance. The results of this calculation are summarized by Figure 18, which shows the dependance of 2-, 3-, and infinite-bandgap cell efficiency on temperature for concentration factors of 1 and 1000. The figure indicates that these schemes can enable very high conversion efficiencies to be achieved at low cell operating temperatures (< 40K), but also again clearly demonstrates that a concentration factor of over a 1000 is necessary to increase the cell operating temperature to between 80 and 100K. For the most optimistic situation an ideal two-bandgap cell has an estimated efficiency of 5 - 6% at 100K with a slight increase in efficiency of only 2% being projected for a more complex three-bandgap power cell. Additionally, calculations of the power cell efficiency which include the more practical

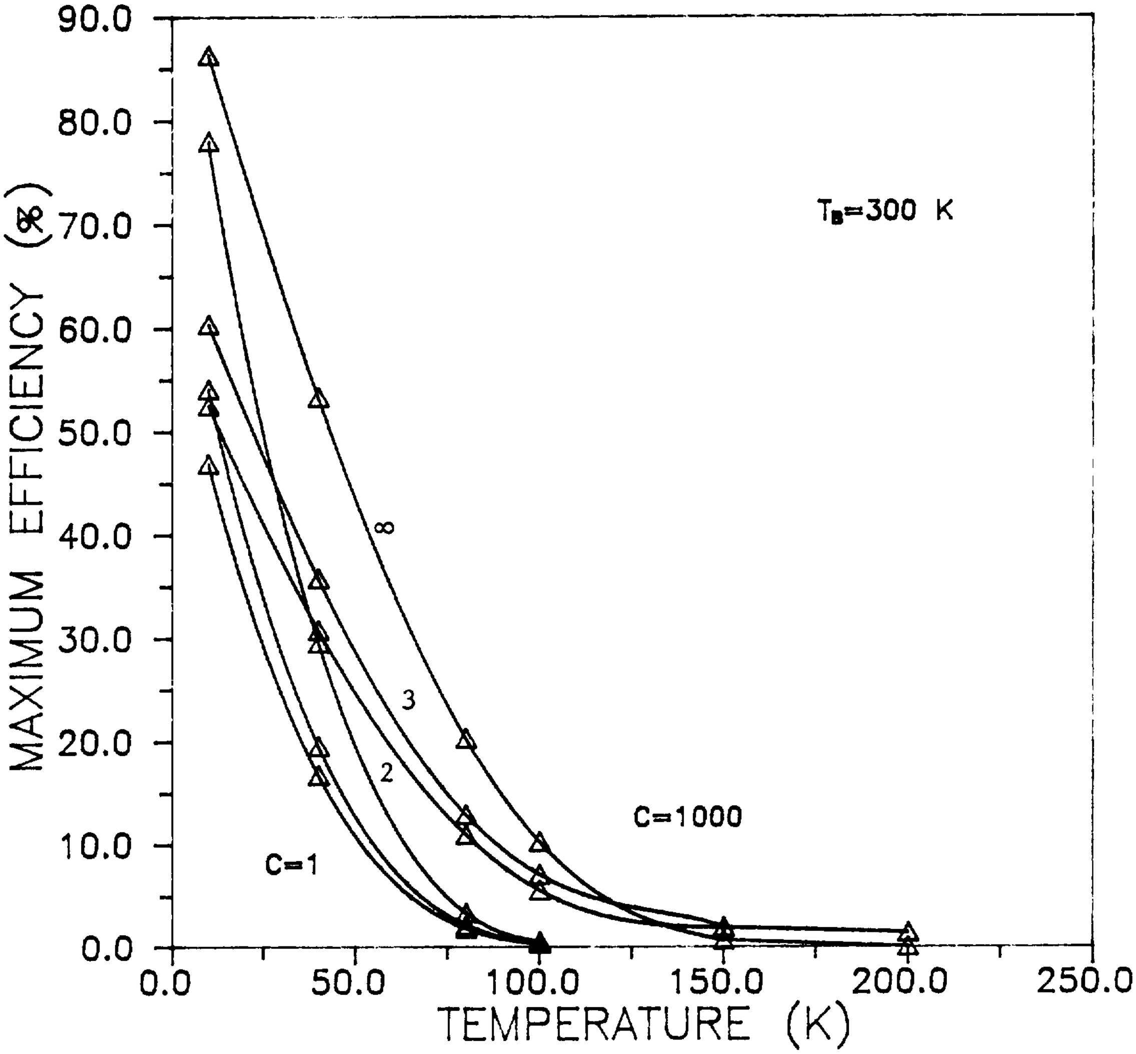

Figure 18. Maximum efficiency for multi-bandgap power cell combinations as a function of cell temperature and radiation concentration factor.

situation of including all the device currents (Equation 39) indicates that very stringent material requirements are needed to realize these values.

## 2.5 Model Calculation for a Heterojunction Power Cell.

In the heterojunction solar cell proposed by Pearsall[20] light enters the p-n diode from the wide bandgap side. Thus photons with energies greater than $E_{G2}$ are absorbed by the top p-type layer and photons with energies between $E_{G2}$ and $E_{G1}$ by the smaller bandgap n-type layer. When $E_{G2} \geq 2E_{G1}$ a photon excited electron in the wide bandgap material has sufficient potential energy to impact ionize a second electron-hole pair on the low bandgap side of the cell as its crosses the interface. Thus for 100% ionization the effective quantum efficiency of photons with energies greater than $E_{G2}$ is two. However, it should be noted that the open cell voltage of the heterojunction is still limited by the smaller bandgap material.

The effective increase in photo-collection efficiency for this cell structure is then given by:

$$\eta_{ph}(E_{G1}) = \int_{E_{G1}}^{\gamma E_{G1}} \frac{dn_{ph}}{dE} \bullet dE + g \bullet \int_{E_{G2}}^{\infty} \frac{dn_{ph}}{dE} \bullet dE \qquad (54)$$

Where $\gamma$ is the ratio of the bandgap energies and g is the impact ionization efficiency. Thus

$$\gamma = \frac{E_{G2}}{E_{G1}} \geq 2,$$

and

$$1 < g \leq 2.$$

To calculate the efficiency of this structure the same procedures as discussed previously were used. Except that in this calculation Equation 41 is replaced by Equation 54 and the open cell voltage is calculated only for the small bandgap (n-type) side of the cell, as this controls the built-in voltage of the heterojunction.

### **2.5.1 Heterojunction Results.**

Figure 19 shows the efficiency calculation for the superlattice avalanche photodiode solar cell as calculated by the above approach. In this calculation ideal collection conditions are assumed and values of $\gamma = 2$ and $g = 2$ are used. For both 1 and 1000 power concentrations little enhancement over the homojunction was observed for cells with bandgap energies greater than 0.125 eV. This is because as shown by Figure 10 there are very few photons with energies above 0.25 eV. However, as the energy gap decreases below 0.125 eV more photons with energies greater than twice the bandgap energy are absorbed which can impact ionize and double the effective number of electrons contributing to the photo-current. Figure 19 shows that as $E_G$ goes to zero the total gain in the effective number carriers collected is doubled in the APD-solar

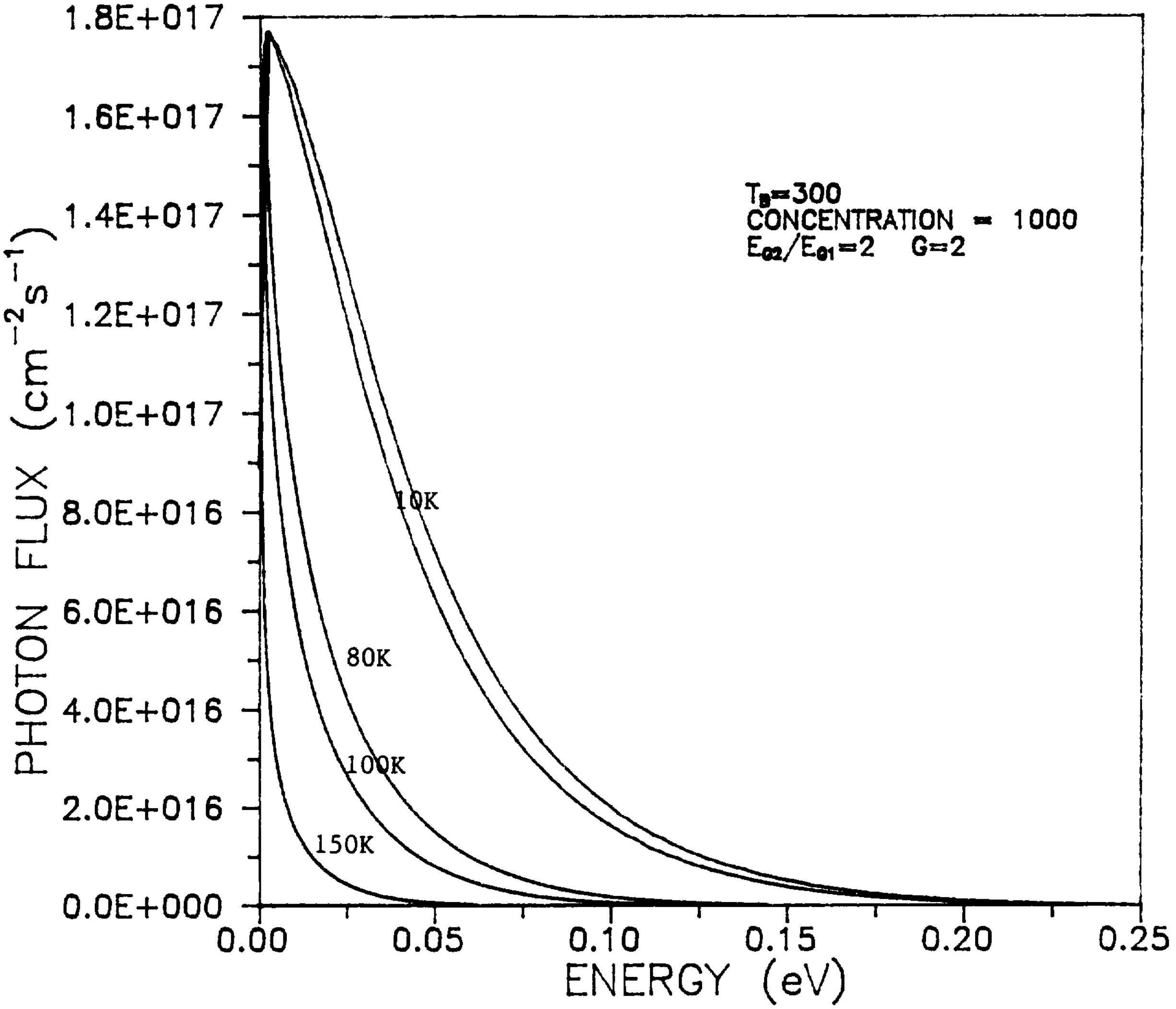

Figure 19. Equivalent photon concentration versus energy for heterojunction (g = 2, $\gamma$ = 2) terrestrial power cell operating at temperatures of 10, 80, 100 and 150K for a concentration factor of 1000.

cell design. This improvement in collection efficiency occurs for both 1 and 1000 power concentration factor. The figure also demonstrates, when compared to Figure 15, that for low bandgap energies the effective work done by the cell increases due to the increased photon collection. This effect is very pronounced for high (1000) concentration and low (10K) temperatures as shown by Figure 19.

The dependence of the efficiency of the APD-solar cell on the bandgap energy, $E_{G1}$, of the smaller bandgap is shown in Figure 20. From these curves it is shown that for a concentration of 1000 maximum efficiencies of 50.1 and 8.1% are obtained when $E_{G1} = 0.045$ and 0.0925 eV and for temperatures of 10 and 80 K, respectively. A comparison between Figures 14 and 20 shows that for bandgap energies greater than 0.125 eV both the conventional and avalanche solar cell have the same efficiencies. Thus it is only for smaller bandgap cells with values of $E_{G1}$ less than 0.125 eV that appreciable increases in performance are realized.

The effect of decreasing the multiplication ratio from 2.0 causes both the peak efficiency and the optimum bandgap energy decrease uniformly towards the curve shown for a simple homopolar junction. Basically, therefore, the avalanche photodiode solar cell collects twice the number of $E_{G1}$ photons for ideal ($\gamma$ = 2, g = 2) conditions and responds in a manner similar to increasing the collection efficiency.

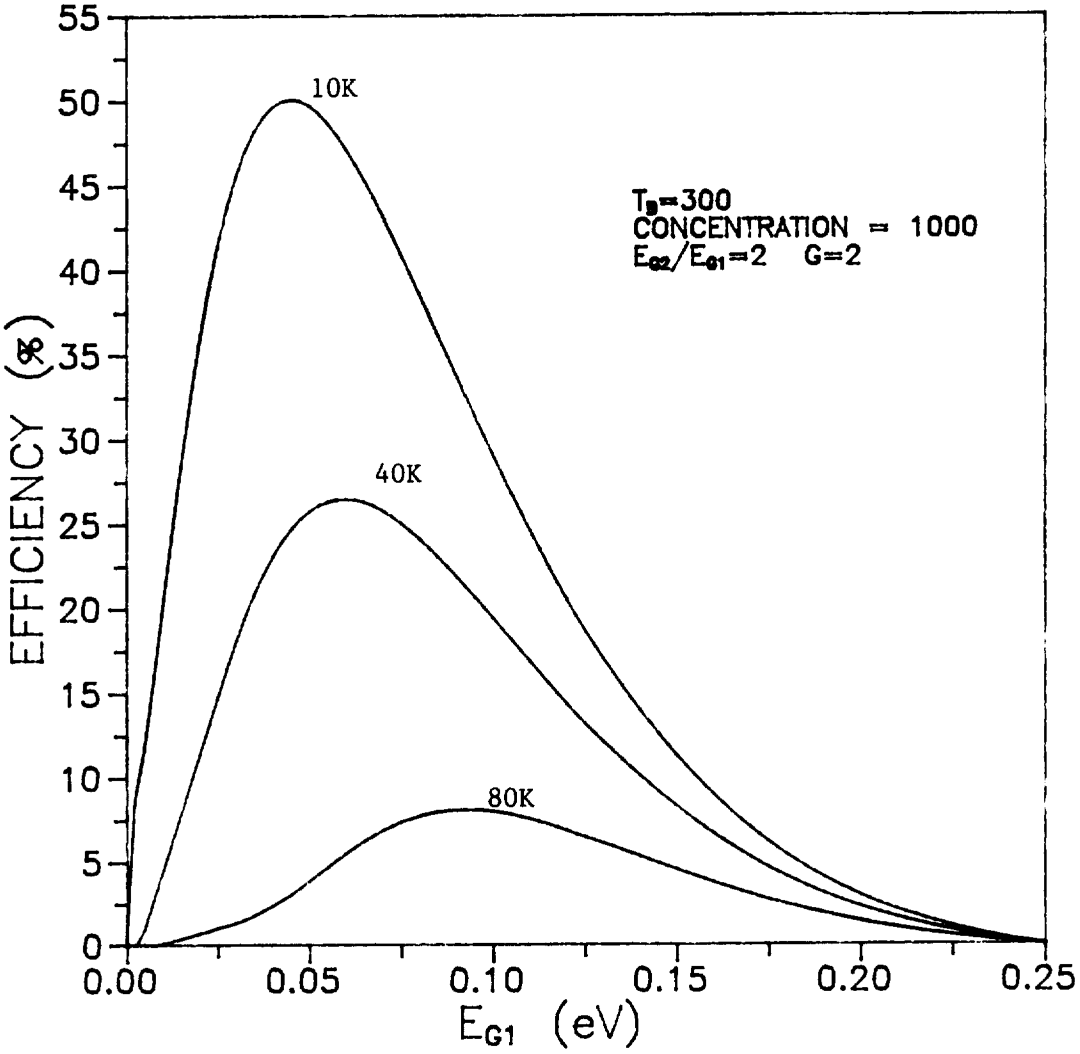

Figure 20. Ideal heterojunction ($g = 2$, $\gamma = 2$) terrestrial power cell efficiency as a function of bandgap energy, $E_{G1}$, for operating temperatures of 10, 40 and 80 K at 1000 concentration.

## 2.6 Calculation for HgCdTe Power Cell and Power Beaming

To conclude this study calculations were also performed for a practical $n^+$-p homopolar HgCdTe power cell in which the device currents discussed in Section 2.3 were included in the total device current as described by equation 39. For this calculation a 10 $\mu$m thick power cell was assumed with $n=10^{18}$ cm$^{-3}$ and $p=10^{15}$ cm$^{-3}$. The analysis showed that for the practical temperature region of interest the diffusion current dominated and increased rapidly with temperature due to the strong dependence of the excess electron lifetime and electron concentration. Figure 21 shows the calculated efficiency for this situation as a function of bandgap energy for the homojunction and heterojunction schemes described previously. As indicated in the figure, the maximum efficiencies obtained at 40 K are 8.4 and 9.5 percent for the homojunction and heterojunction cases, respectively. With increasing temperature, the efficiencies decrease very rapidly to less than 2 percent at 80 K. Therefore, these calculations show the severe limitations of this concept.

Calculations were also carried out to determine the feasibility of using a laser to beam power from earth to satellite or satellite to satellite. To obtain the proper spectral distribution, the photon flux in Equation 40 was replaced with a $\delta$-function at the energy (0.25 eV) corresponding to the operating wavelength ($\lambda$ = 5.3 $\mu$m) of a CO laser. This wavelength falls within one of the atmospheric transmission windows and thus would allow earth to satellite operation. The intensity of the $\delta$-

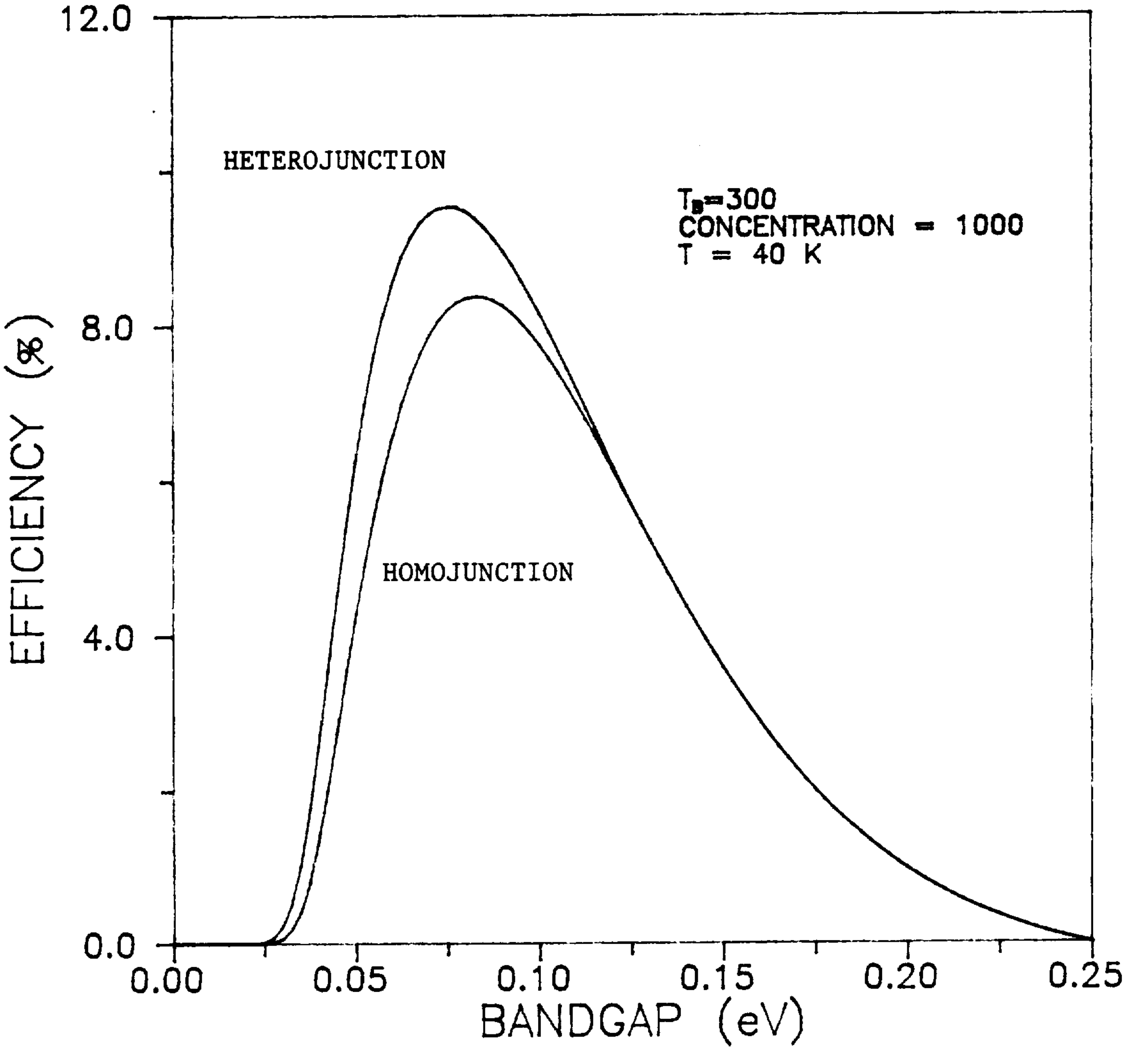

Figure 21. Efficiency of homojunction and heterojunction HgCdTe power cells at 40 K as a function of bandgap energy for calculations including device currents.

function was adjusted so that the total incident power density, as determined by Equation 42, was 1 w/cm$^2$. Efficiency calculations were then carried out as previously described for the single bandgap power cells. However, the effect of the device currents as described in Section 2.3 was also included in the calculation for a 10$\mu$m thick power cell. Figure 22 shows the calculated efficiencies as a function of energy bandgap for power cell temperatures of 150 and 200K. As expected, for bandgap energies greater than that of the CO laser radiation, the efficiency decreases to zero. The 150 and 200K power cells demonstrate peak efficiencies of 31 and 8.5 percent, respectively.

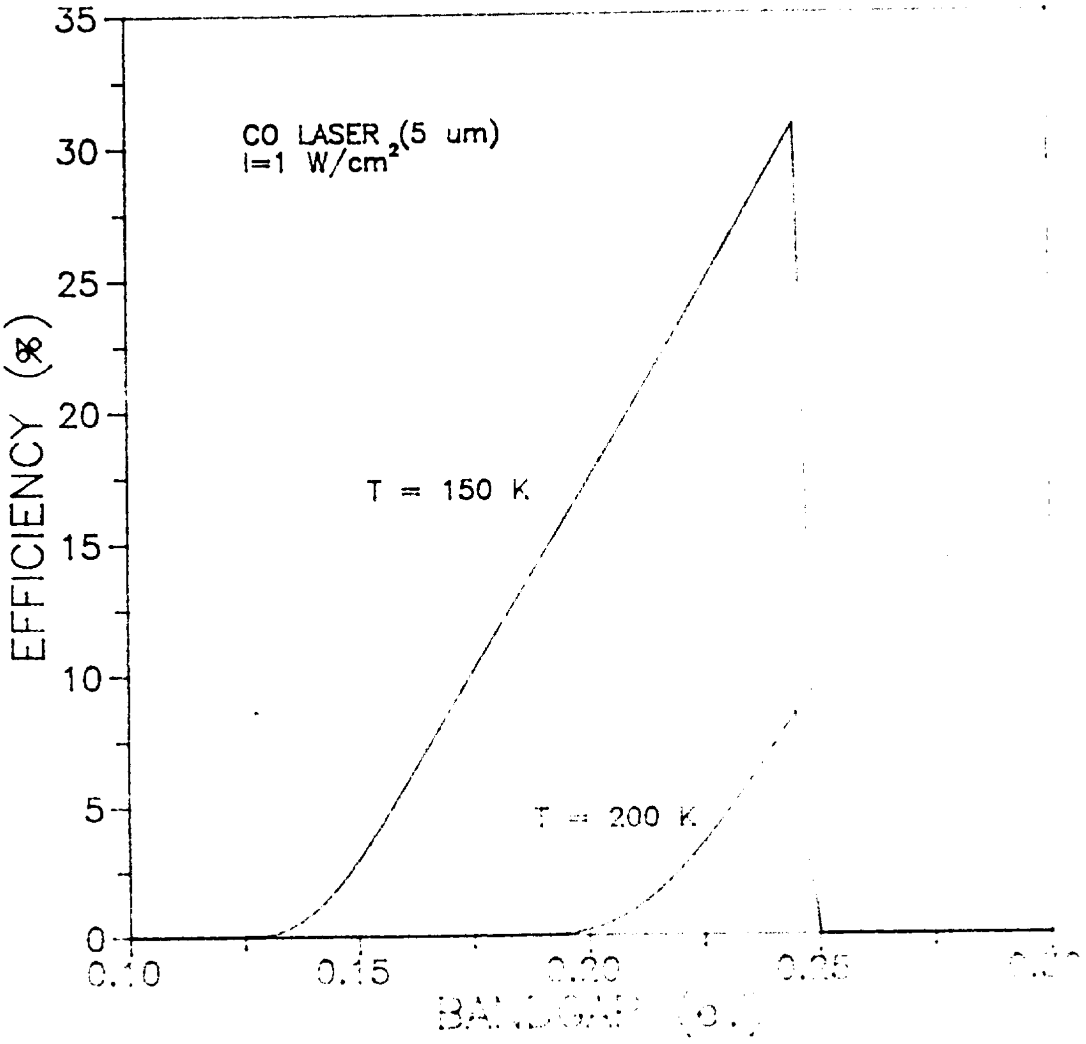

Figure 22. Efficiency of single bandgap power cell including diffusion current effects versus bandgap energy for operating temperatures of 150 and 200K under CO laser irradiation of 1 W/cm$^2$.

# 3. MATERIAL DEVELOPMENT

The growth of $Hg_{1-x}Cd_xTe$ alloys by molecular beam epitaxy demands special considerations because of the following properties unique to this material system:[21-23] 1) $Hg_{1-x}Cd_xTe$ with x-values between 0.3 and 0.2 decompose very rapidly and non-congruently above 150°C;[24] 2) the sticking coefficient of Hg is very low, <0.03;[25] and 3) the vapor pressure of Hg is very high.[26] Because the decomposition rate of $Hg_{1-x}Cd_xTe$ alloys decreases rapidly with decreasing temperature, the first consideration can be elevated to some extent by growing at low substrate temperatures. However, there is a lower limit placed on the substrate temperature which is determined by the need to grow single crystal material. Essentially, the substrate temperature must be high enough for the absorbed molecules (Hg, Cd and Te) to have sufficient energy to migrate along the growth surface so that they solidify in the lowest energy configuration, i.e. form a single crystal. This temperature must be found experimentally and is expected to be near 200°C. The lower substrate temperature is also expected to increase the Hg sticking coefficient.

The low sticking coefficient and high vapor pressure of Hg also places special demands on both the design and operation of the MBE system. Firstly, because of the low sticking coefficient, most of the Hg flux is not absorbed on the substrate. Thus, a very high ($> 10^{17}$ $cm^{-2}s^{-1}$) and continuous Hg-flux density is required to grow low x-valued $Hg_{1-x}Cd_xTe$ layers that are sufficiently thick (> 10 microns) for infrared detector and terrestrial power cell applications. This makes it essential to use elemental Hg for the Hg-source because a binary compound such as HgTe, will be quickly depleted. Secondly, the high vapor pressure of Hg at room temperature makes it impossible to use as a conventional MBE source material. Either the Hg must be kept at very low temperatures during most of the system operation, or it must be introduced into the high vacuum chamber during the growth cycle. Because the first approach makes the Hg source very susceptible to contamination and would require repeated openings of the system to replenish the Hg charge, the second option was initiated in this work. Lastly, the high Hg vapor pressure makes it essential to have extensive cryoshielding through out the system and an effective pumping system to limit and quickly remove the excess Hg-vapor during growth and the post-growth bake-out procedure.

An estimate of the critical control parameters required to growth $Hg_{1-x}Cd_xTe$ alloys can be deducted from the relative magnitudes of the sticking coefficients for elemental Hg, Cd and Te. Because Cd and Te have high, near unity sticking coefficients, most of the incident Cd and Te molecular beams will be deposited on the substrate. Thus, the magnitude of the Te flux will determine the anion-to-cation ratio and, therefore, the growth rate. Because of the large difference between the sticking coefficients of Hg and Cd, the Cd will always be preferentially absorbed. Thus, provided the Hg is in excess, the Cd flux will determine the composition of the alloy. To first order, the control of the growth process is therefore dependent on the flux control of the Te and Cd ovens and the stability of the substrate temperature. Ideally, it is desired that upon condensation on the substrate all three components should be in precise balance to form a crystalline, homogeneous layer that is in exact stoichiometric balance.

The apparatus designed to investigate the MBE growth requirements for HgCdTe is shown in Figure 23. The system consists of three principal components, a growth chamber, a sample load-lock, and a pumping system. All were constructed from stainless steel and sealed with copper gaskets. The main component of the growth chamber is the furnace module which was cooled to liquid nitrogen temperatures and can hold up to six furnaces. To minimize cross-contamination between the ovens, the growth furnace module was mounted horizontally and the cryoshielding enclosed as much as possible of the ovens. The furnace shutters were also cooled through their mountings on the cryo-shielding and were actuated externally by rotatable feed throughs. The solid state furnaces were of conventional design and lined with high purity graphite. Their temperatures were controlled and stabilized to a precision of 0.1°C by using-highly stabilized d.c. power supplies and precision temperature controllers. To provide the flux density and the furnace operational time necessary to grow thick layers, the Hg-furnace was split into two components, an oven-section to provide the flux control and a large reservoir. The Hg furnace has a stainless steel lining and is fitted with a small probe to monitor

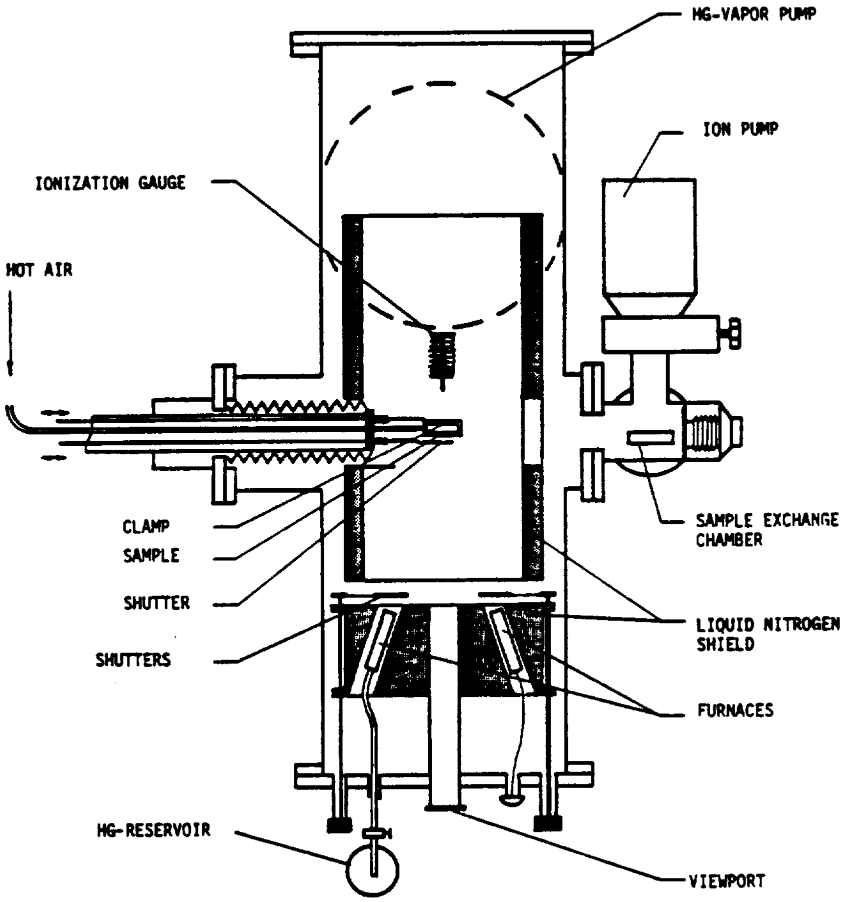

Figure 23. Schematic of MBE apparatus used to grow CdTe and $Hg_{1-x}Cd_xTe$ layers.

the Hg level. The principal feature of the reservoir is a stainless steel bellows which was attached to a micrometer so that the reservoir volume could be precisely reduced to feed Hg into the oven section.

Because the substrate temperatures required for the growth of HgCdTe were expected to be below 300°C and must be well regulated and uniform, a heated air flow system was used. This system had a temperature stability of <0.1°C and allowed the substrate temperature to be abruptly changed by altering the air mix, or if necessary, to be cooled below room temperature. As shown, the air flow system was mounted externally and connected to the substrate holder through a metal bellows. Samples were loaded by extending the bellows so that the sample holder enters the transfer chamber on the other side of the system.

The vacuum system consists of a sorption pump and an ion-pump for the sample load-lock module, and a sorption pump and Hg-vapor diffusion pump fitted with two liquid nitrogen cold traps for the growth chamber. These systems typically produced vacuums in the $10^{-7}$ and $10^{-9}$ torr range, respectively, which were sufficient for the initial investigations of the crystalline properties of CdTe and HgCdTe. The system was operated by first loading a sample into a cassette in the load-lock module and pumping until a vacuum of $<10^{-7}$ torr was obtained. The load-lock valve was then opened and the sample holder extended into the load-lock where a sample was transferred and clamped into it. The sample holder was then withdrawn into the growth chamber, the load-lock valve closed, and the growth chamber pumped back down to <$10^{-8}$ torr. During the preliminary bake-out and stabilization of the binary and elemental furnaces, the sample was protected by covering it with a portion of the shutter. Once the CdTe furnace temperature had stabilized, the sample surface was exposed and heated to remover any surface contaminants. Following the thermal etch the CdTe furnace shutter was opened and a CdTe buffer layer grown. To grow HgCdTe the sample surface was first protected as described previously and the Cd and Te flux rates set using an ionization gauge and adjacent to the growth position. The Hg furnace temperature was then raised to the required setting for the run, and the bellows compressed to pipette Hg into the furnace. After the Hg furnace temperature had stabilized, the sample was uncovered and the Hg, Cd and Te shutters opened to commence growth. During the running of the Hg-furnace, the Hg level was continuously monitored and kept constant by the use of a small probe which formed an electrical make-and-break switch with the surface of the Hg. This procedure was believed to result in a more constant flux density by maintaining a constant flux geometry and by reducing variations in the thermal loading on the furnace. The growth run was terminated by closing the Cd and Te furnace shutters and cooling the sample in the Hg flux to protect the surface. Mercury was removed by expanding the metal bellows of the Hg reservoir so that all the Hg is withdrawn from the furnace. The sample surface could also be protected by epitaxially depositing a thin layer of CdTe.

In order to obtain the best substrate surface conditions for the MBE growth of HgCdTe and to determine the conditions for growing CdTe-HgCdTe heterostructures and CdTe-HgTe superlattice structures, the crystalline properties of epitaxial layers of CdTe on bulk CdTe substrates were first examined. The CdTe substrates used in this work were orientated within 0.5° of the <111> direction, polished on the A face, and typically had dislocation densities in the $10^5$ - $10^4$ $cm^{-2}$ range. Before growth they were degreased and cleaned by sequential rinses in trichlorethylene, methanol, and D.I. water and then etched for 2 min. in a 1% Br-methanol solution to remove a 25 micron surface layer. After further rinses in methanol and Di water, they were blown dry with dry nitrogen gas and bonded to Mo holders using pure In. The final surface preparation was performed in the growth chamber and consisted of a thermal etch at 350°C for 10 min. It was estimated that this procedure removed any hydrocarbon contamination on the surface. Simultaneously with the substrate cleaning, the CdTe furnace was baked out and its temperature set to give a growth rate of 2 micron/h.

Following these initial growth runs and characterizations, HgCdTe layers were grown on epitaxial grown CdTe buffer layers, 2-3 microns thick. These growths were performed for substrate temperatures between 180-200°C and constant Te and Hg flux rates. The Te flux rate was the same as used to grow CdTe and the Cd flux was reduced in small increments from the level required to grow stoichiometric CdTe. The Hg flux rate was kept constant and was approximately two orders of magnitude larger than either the Te or

Cd flux rates. The crystallographic properties of these layers were very similar to those reported for CdTe. The HgCdTe layers were approximately 3 microns thick and their composition and homogeneity was determined from infrared transmittance measurements. The transmission data taken on three samples are shown in Figure 24. The transmission cut-on of the layers is observed to move to longer wavelengths from 0.8 to 2 microns as the Cd flux density is decreased, showing that the Hg composition in the layer is increasing. For these alloys an absorption coefficient of 500 $cm^{-1}$ is expected at the energy bandgap. This corresponds to a transmission of 30% for a 3 micron layer. Thus, the energy bandgaps are calculated to occur at 1.38, 0.81, and 0.58 eV, corresponding to alloy compositions with x-values of approximately 0.9, 0.85 and 0.5, respectively. Since this initial work an CBE system for the growth of HgCdTe has been constructed at Georgia Tech and used to grow high quality long-wavelength HgCdTe materials that are ideally suited for this or related applications.

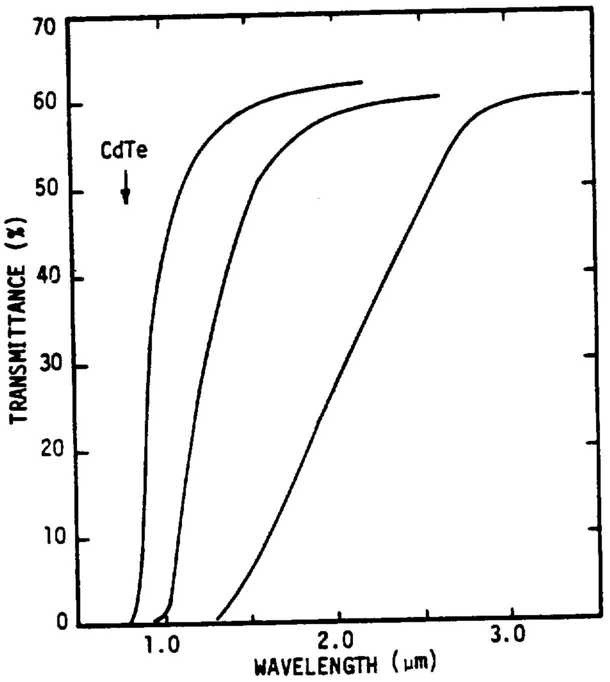

Figure 24. Infrared Transmittance Spectra of MBE Grown $Hg_{1-x}Cd_xTe$ layers.

# 4. CONCLUSIONS

In this study a detailed characterization has been made of the effectiveness of a HgCdTe terrestrial power cell to directly convert the long-wavelength radiation emitted by the earth into electrical power. To perform this study required the development of a complete parameter data set for the HgCdTe alloy system in order to accurately determine the compositional and temperature dependences of the alloy carrier concentrations, lifetimes and diffusion lengths. This analysis showed that p-type HgCdTe alloys should have superior photoconductive properties than n-type doped alloys and that an abruptly doped $n^{+}$-p junction should be the optimum diode structure for enhancing power cell performance. By extending the theory first developed by Henry to this situation the maximum efficiencies possible for single, multiple and heterojunction cells was calculated for radiation concentration factors up to 1000 as a function of the cell operating temperature. This calculation also defined the bandgap energies required to achieve the predicted performance. As described fully in the text, very high conversion efficiencies can be achieved for low power cell temperatures (< 40K), but for the practical operating temperatures of a earth orbiting satellite (175-225K) the efficiencies are very low. The use of high concentration factors of up to 1000 and multiple bandgap was demonstrated to enable efficiencies of 5-6% at a cell temperature of 100K for an ideal cell structure. Unfortunately, this efficiency value is only marginal and can only be achieved at a temperature significantly below that required for this application. The incorporation of the device currents into this calculation was also performed and showed that very stringent material properties are required for this application and that even if achieved would still further reduce the obtainable efficiencies. As a consequency of this study no further work was recommended on this project.

Coincident with these analysis some preliminary material studies were performed using an MBE system specifically designed for the growth of HgCdTe alloys. This system was used to grow CdTe and $Hg_{1-x}Cd_xTe$ layers with $0.9 > x > 0.5$. Investigation of the properties of these layers show that at present the quality of CdTe substrates and/or surface preparation procedures cause an initial degradation of the quality of the layer, but that these defects can be grown out. For CdTe layers thicker than 5 microns, good quality surfaces were obtained. Epitaxial deposited CdTe was shown to be remarkably adaptable and good quality CdTe layers have been grown. Preliminary growth runs produced good quality $Hg_{1-x}Cd_xTe$ layers with x-values between 0.9 and 0.5 with spectral response characteristics extending out to 2 microns. Since this work HgCdTe alloy compositions with bandgap energies very close to those required for a terrestrial power cell have been grown at Georgia Tech with characteristics that demonstrate that the basic material properties can be achieved for this application using thin film growth techniques.

# 5. REFERENCES

1. C.H. Henry, "Limiting Efficiency of Ideal Single and Multiple Energy Gap Terrestrial Solar Cells," J. Appl. Phys. 51, 4494 (1980).
2. E.O. Kane, "Band Structure of Indium Antimonide," J. Phys. Chem. Solids 1, 249-261 (1957).
3. J.L. Schmit and E.L. Stelzer, "Temperature and Alloy Compositional Dependences of the Energy Gap of $Hg_{1-x}Cd_xTe$," J. Appl. Phys. 40, 4865-4869 (1969).
4. Y. Guldner, C. Rigaux, A. Nycielski and Y. Couder, "Magnetooptical Investigation of $Hg_{1-x}Cd_xTe$ Mixed Crystals," Phys. Stat. So. (b) 82, 149-158 (1977).
5. R. Dornhaus and G. Nimtz, "The Properties and Applications of the $Hg_{1-x}Cd_xTe$ Alloy System," Springer Tracts in Modern Physics Ed. G. Hohler, (1976).
6. M.H. Weiler, R.L. Aggarwal and B. Lax, "Interband Magnetoreflectance in Semiconducting $Hg_{1-x}Cd_xTe$ Alloys," Phys. Rev. B.
7. J. Baars and F. Sorger, "Reststrahlen Spectra of HgTe and $Cd_xHg_{1-x}Te$," Solid State Commun. 10, 875-877 (1972).
8. G.L. Hansen and J.L. Schmitt, J. Appl. Phys. 54, 1639 (1983).
9. S.L. Lehoczky, C.J. Summers, F.R. Szofran and B.G. Martin, "Electrical Characterization of $Hg_{1-x}Cd_xTe$ Alloys, Proceedings of Materials Processing in the Reduced Gravity Environment of

Space," Boston 1981, Materials Research Society Vol. 9., Ed. Guy E. Rindone. North-Holland, New York, pp. 421-431, (1982).

10. W. Scott, "Electron Mobility in $Hg_{1-x}Cd_xTe$," J. Appl. Phys. 43, 1055-1062 (1972).

11. A.R. Beattie, "Quantum Efficiency in InSb," J. Phys. Chem. Solids. 23, 1049-1056 (1962).

12. R.N. Hall, "Recombination Precesses in Semiconductors," Proc. Inst. Elec. Eng., Supp. B 106, 923 (1959).

13. A.R. Beattie and P.T. Landsberg, "Auger Effect in Semiconductors," Proc. Roy. Soc. 249, 16-29 (1958).

14. T.N. Casselman and P.E. Petersen, "A Comparison of the Dominant Auger Transitions in p-Type (HgCd)Te," Solid State Comm. 33, 615-619 (1980).

15. A.R. Beattie and G. Smith, "Recombination in Semiconductors by a Light Hole Auger Transition," Phys. Stat. Sol. 9, 577-586 (1967).

16. S.M. Sze, "Physics of Semiconductor Devices," (1969), John Wiley and Sons, New York.

17. C.T. Sah, R.N. Noyce and W. Shockley, "Carrier Generation and Recombination in p-n Junctions and p-n Junction Characteristics," Proc. IRE 45, 1228-1243, (1957).

18. D.A. Evans and P.T. Landsberg, "Recombination Statistics for Auger Effects with Applications to p-n Junctions," Solid State Electronics 6, 169-181 (1963).

19. W.W. Anderson, "Tunnel Current Limitations of Narrow Bandgap Infrared Charge Coupled Devices," Infrared Physics 17, 147-164 (1977).

20. T.P. Pearsall, Zap! Introducing the Zero-Bias Avalanche Photodiode Electronics Letters 18, 512-514 (1982).

21. The 1981 and 1983 U.S. Workshops on the Physics and Chemistry of Mercury Cadmium Telluride. J. Vac. Sci. Technol., Vol. 21 No. 1. (1982) J. Vac. Sci. Technol. (1983).

22. J.P. Fauire and A. Million, "Molecular Beam Epitaxy of II-VI Compounds: $Cd_xHg_{1-x}Te$, J. Cryst Growth, Vol. 54, pp. 582-585 (1981).

23. J.P. Faurie and A. Million, "$Cd_xHg_{1-x}Te$ n-Type Layers Grown by Molecular Beam Epitaxy," Apply. Phys. Lett., Vol. 41, pp. 264-266 (1982).

24. R.F.C. Farrow, G.R. Jones, G.M. Williams, P.W. Sullivan, W.J. Boyle and J.T.M. Woltherspoon, "The Vaporization of $Hg_{1-x}Cd_xTe$ Crystals - a Case of Gross Incongruency," J. Phys. D.: Apply. Phys., Vol. 12, pp. L117-L121 (1979).

25. H. Holloway, D.K. Honke and E.M. Logothetis, "Epitaxial Growth of Small Bandgap Semiconductors," J. Vac. Sci. Technol., Vol. 8, pp. 146 (1971).

26. R.E. Honig and D.A. Kramer, "Vapor Pressure Data for the Solid and Liquid Elements," RCA Review, pp. 285-305 (1969).